

## Mid- to Inner-Shelf Coupled ROMS–SWAN Model–Data Comparison of Currents and Temperature: Diurnal and Semidiurnal Variability

NIRNIMESH KUMAR, FALK FEDDERSEN, AND SUTARA SUANDA

*Scripps Institution of Oceanography, University of California, San Diego, La Jolla, California*

YUSUKE UCHIYAMA

*Department of Civil Engineering, Kobe University, Kobe, Japan*

JAMES MCWILLIAMS

*Institute of Geophysics and Planetary Physics, University of California, Los Angeles, Los Angeles, California*

(Manuscript received 1 June 2015, in final form 16 November 2015)

### ABSTRACT

Accurately representing diurnal and semidiurnal internal variability is necessary to investigate inner-shelf to midshelf exchange processes. Here, a coupled Regional Ocean Model System (ROMS)–Simulating Waves Nearshore (SWAN) model is compared to observed diurnal and semidiurnal internal tidal variability on the mid and inner shelf (26–8 m water depth) near San Pedro Bay, California. Modeled mean stratification is about one-half of that observed. Modeled and observed baroclinic velocity rotary spectra are similar in the diurnal and semidiurnal band. Modeled and observed temperature spectra have similar diurnal and semidiurnal band structure, although the modeled is weaker. The observed and modeled diurnal and semidiurnal baroclinic velocity- and temperature-dominant vertical structures are similar and consistent with mode-one internal motions. Both observed and modeled diurnal baroclinic kinetic energy are strongly correlated to diurnal wind forcing and enhanced by subtidal vorticity-induced reduction in the inertial frequency. The mid- and inner-shelf modeled diurnal depth-integrated heat budget is a balance between advective heat flux divergence and temperature time derivative. Temperature–velocity phase indicates progressive semidiurnal internal tide on the midshelf and largely standing internal tide on the inner shelf in both observed and modeled. The ratio of observed to modeled inferred phase speed is consistent with the observed to modeled stratification. The San Pedro Bay modeled semidiurnal internal tide has significant spatial variability, variable incident wave angles, and multiple local generation sites. Overall, the coupled ROMS–SWAN model represents well the complex diurnal and semidiurnal internal variability from the mid to the inner shelf.

### 1. Introduction

The inner shelf (where the surface and bottom boundary layers overlap, i.e., from 5 to ~15 m depth; e.g., [Lentz and Fewings 2012](#)) and midshelf (with distinct surface and bottom boundary layers, i.e., offshore of the inner shelf to ~50 m depth; e.g., [Austin and Lentz 2002](#)) together

represent the transition region from land to the open ocean. Cross-shelf exchange processes in the inner- and midshelf regions influence pollutant dispersal (e.g., [Boehm et al. 2002](#); [Grant et al. 2005](#)), cross-shelf nutrient exchange and associated nearshore harmful algal blooms (e.g., [Anderson 2009](#); [Omand et al. 2012](#)), and temperature fluctuations through advective heat fluxes (e.g., [Fewings and Lentz 2011](#); [Sinnott and Feddersen 2014](#)). Numerical modeling studies focused on cross-shelf exchange barely resolve the inner-shelf region and focus on subtidal and longer time scales. Accurate simulation of mid- to inner-shelf processes requires a coupled wave and circulation model with wind, wave, tide, and buoyancy processes along with adequate grid resolution.

 Denotes Open Access content.

*Corresponding author address:* N. Kumar, Scripps Institution of Oceanography, University of California, San Diego, 9500 Gilman Dr., La Jolla, CA 92093-0209.  
E-mail: n2kumar@ucsd.edu

DOI: 10.1175/JPO-D-15-0103.1

Recently, [Kumar et al. \(2015, hereinafter K15\)](#) simulated waves and circulation from the surfzone through the midshelf region near Huntington Beach, California, in the San Pedro Bay (SPB) with the coupled Regional Ocean Modeling System (ROMS)–Simulating Waves Nearshore (SWAN; [Warner et al. 2010](#)) that included buoyancy, wind, tide, and wave forcing. The model was evaluated, with focus on subtidal time scales, by statistical comparison of waves, circulation, and temperature observations on a 4-km-long cross-shore transect spanning the surfzone to the midshelf as part of the August to October 2006 Huntington Beach (HB06) experiment. Overall, the coupled ROMS–SWAN model well represents the surface gravity waves and subtidal circulation dynamics from the midshelf to the surfzone.

In addition to subtidal variability, tidal-band internal variability also affects cross-shelf exchange on the mid and inner shelf. The semidiurnal internal tide on the inner-shelf induces heat and nitrate fluxes (e.g., [Lucas et al. 2011](#); [Wong et al. 2012](#)). Internal waves pump nutrients up into the euphotic zone, initiating phytoplankton blooms ([Omand et al. 2012](#)) and inducing larval transport ([Pineda 1999](#)). Cold waters are advected by nonlinear internal waves across the shelf (e.g., [Pineda 1994](#); [Nam and Send 2011](#)) all the way into the surfzone ([Sinnott and Feddersen 2014](#)). On the SPB mid- to inner-shelf region, significant diurnal and semidiurnal internal variability is observed (e.g., [Noble et al. 2009](#); [Wong et al. 2012](#); [Nam and Send 2013](#)), advecting phosphate- and nitrate-rich subthermocline water to the nearshore ([Wong et al. 2012](#); [Omand et al. 2012](#)).

At the critical latitude ( $\sim 30^\circ\text{N}$ ) where the inertial ( $f$ ) and diurnal (1 cpd) frequencies coincide, diurnal sea-land breeze (SLB) forcing on the shelf leads to a strong diurnal clockwise-rotating (in the Northern Hemisphere) internal response in both observations ([Simpson et al. 2002](#); [Zhang et al. 2009](#)) and three-dimensional ocean models ([Zhang et al. 2010](#)). North of the critical latitude (i.e.,  $f > 1$  cpd), strong diurnal-band internal motions have been observed in the Southern California Bight ([Lerczak et al. 2001](#); [Beckenbach and Terrill 2008](#); [Cudaback and McPhee-Shaw 2009](#)), including the HB06 study region ([Nam and Send 2013](#)), and attributed to both the subtidal vorticity reducing the effective inertial frequency below diurnal (e.g., [Lerczak et al. 2001](#)) and direct forcing by diurnal barotropic tides (e.g., [Beckenbach and Terrill 2008](#)). However, the principal driver for strong diurnal internal motion in the SPB is not understood yet, and a three-dimensional model has not been shown to effectively reproduce this shelf diurnal-band internal variability poleward of the critical latitude and dependence on effective inertial frequency. A model that accurately represents internal diurnal variability can be used to simulate exchange processes.

Semidiurnal internal tides are a ubiquitous source of temperature and velocity variability on continental shelves (e.g., [Leichter et al. 1996](#); [Lerczak et al. 2003](#); [Mackinnon and Gregg 2003](#); [Inall et al. 2011](#); [Suanda and Barth 2015](#)). They are locally generated by the barotropic tide interacting with a stratified continental slope or shelf break (e.g., [Huthnance 1989](#); [Noble et al. 2009](#)) or remotely generated and propagate onto the shelf (e.g., [Nash et al. 2012](#)). ROMS (hydrostatic) modeling studies have characterized the generation and dissipation of the semidiurnal internal tide in the Southern California Bight ([Buijsman et al. 2012](#)) and on the Oregon continental slope ([Osborne et al. 2011](#)). Similar semidiurnal internal tide generation and dissipation in Monterey Bay were identified with nonhydrostatic models ([Jachec et al. 2006](#)). Multiple local and remotely generated sources result in semidiurnal internal tide spatial variability and variable or multiple incidence angles ([Suanda and Barth 2015](#)). Furthermore, outer- to midshelf semidiurnal internal tides are a mix of purely progressive and standing internal waves ([Winant and Bratkovich 1981](#); [Rosenfeld 1990](#); [Lerczak et al. 2003](#)). Previous modeling studies with grid resolution  $\geq 250$  m do not well resolve the mid- and inner-shelf region, and reproduction of semidiurnal internal variability from the mid to inner shelf using three-dimensional models has not been considered. To study internal tide-induced cross-shelf exchange on the mid to inner shelf, a high-resolution model with realistic bathymetry, boundary conditions, and forcing must first be tested against field observations. A tested model can provide insight into generation sites and cross-shelf transformation of internal motion.

This companion paper to [K15](#), which examined subtidal variability, focuses on model–data comparison of diurnal and semidiurnal internal variability in the mid- to inner-shelf region near Huntington Beach, California. Model–data comparison of barotropic tidal processes were conducted in [K15](#) and suggest that diurnal barotropic tidal constituents are well modeled, while semidiurnal barotropic tidal constituents are underestimated by approximately one-third. The HB06 field experiment observations are described in [section 2a](#). The coupled ROMS–SWAN model is described in [section 3](#). Statistical model–data comparison is performed on diurnal- and semidiurnal-band internal currents and temperature variability in [section 4](#). The observed and modeled relationship between diurnal-band baroclinic kinetic energy, diurnal wind forcing, diurnal barotropic tides, and effective Coriolis frequency is examined in [section 5a](#), and depth-integrated diurnal-band heat budget from inner to midshelf is examined in [section 5b](#). The coherence and phase between semidiurnal velocity and temperature variability at and across moorings is used to examine the progressive or standing nature of the semidiurnal internal

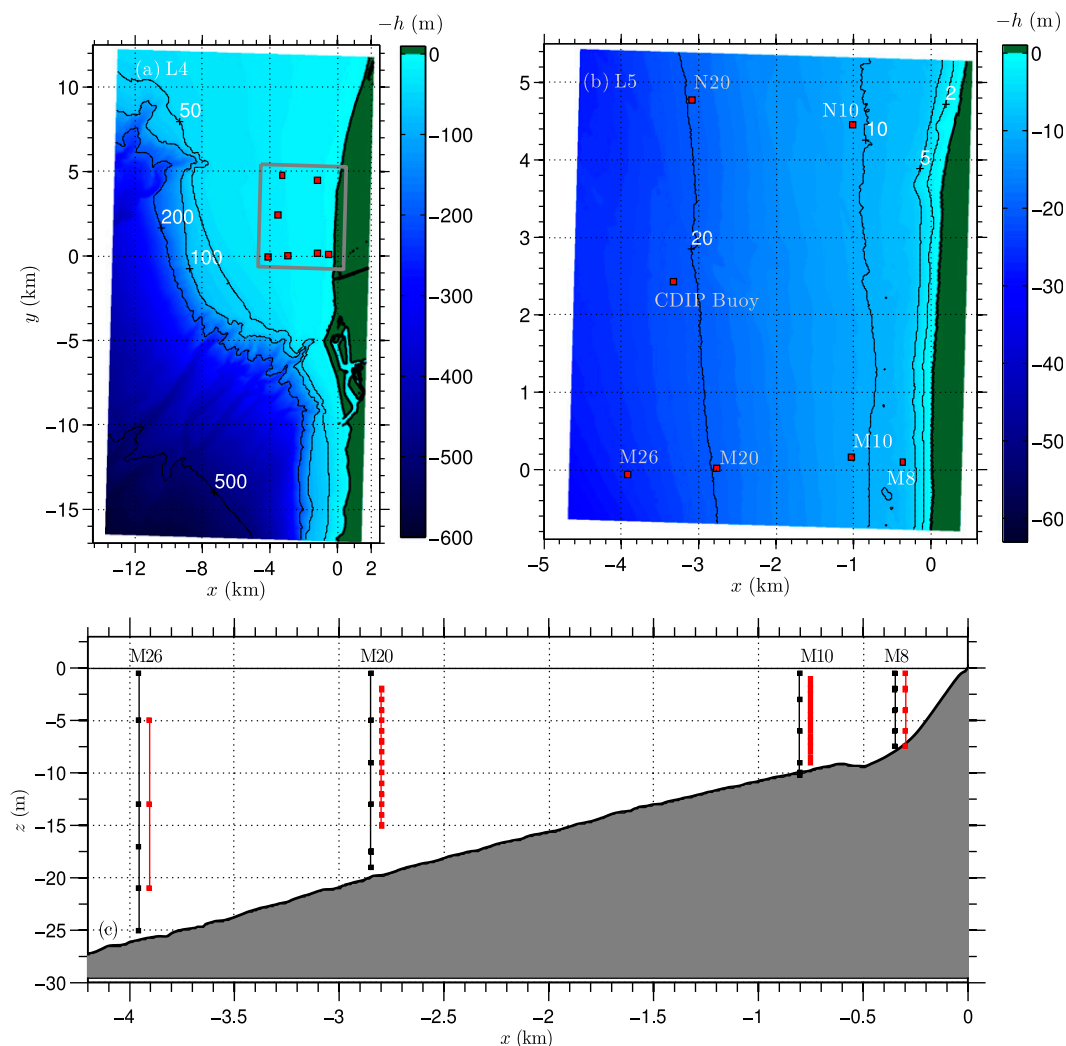


FIG. 1. Model grids showing (a) outer shelf to inner shelf and (b) midshelf to surfzone region adjacent to Huntington Beach and Newport Beach in the SPB. The color shading represents the bathymetry, while red squares show the location of offshore moorings, CDIP wave buoy, and a surfzone frame. These grids have a resolution of 50 m (L4) and 10 m (L5). Note the water depth  $h$  is a negative number in these figures. The HB06 instrument schematic is shown through a (c) cross-shore transect at  $y = 0$  m with the shelf and nearshore bathymetry ( $h < 30$  m) with cross-shelf and vertical instrument locations of thermistors (black) and velocity (red) indicated. The vertical coordinate  $z = 0$  m is at mean sea level and positive upward. The bathymetry  $h(x, y)$  is from the NOAA Tsunami DEM (Caldwell et al. 2011).

tide (section 5c). Finally, semidiurnal baroclinic energy fluxes and their divergence are examined over the model domain at different times to highlight the variable sources and incidence angles of the semidiurnal internal tide (section 5d). The results are summarized in section 6.

## 2. Observations and methods

### a. HB06 experiment description

During the HB06 experiment (Clark et al. 2010, 2011; Omand et al. 2011, 2012; Nam and Send 2011; Feddersen

et al. 2011; Feddersen 2012; Rippy et al. 2013; K15), currents, waves, temperature, and sea surface elevation were measured on a cross-shore transect from the surfzone to the midshelf adjacent to Huntington Beach, California (Fig. 1). The observations and methods are described in detail in K15 and are summarized here. The bathymetry within 4 km from the transect is alongshore uniform, while over length scales  $>10$ -km bathymetry is complicated because of rapidly varying shelf width. The right-handed coordinate system is defined such that positive cross shore ( $x$ ) is directed onshore ( $34^\circ$  true north) with  $x = 0$  m at the shoreline,  $y$  represents the

TABLE 1. List of midshelf to surfzone HB06 experiment cross-shore transect instrument sites, depth, deployment duration, and cross-shore ( $x$ ) location.

Site	Mean depth (m)	Deployment duration (days)		Cross-shore location (m)
		Temperature	Velocity	
M26	26	86	86	-3950
M20	20	60	86	-2850
M10	10	84	86	-800
M8	8	85	85	-348

alongshore, and  $z$  is positive upward with  $z = 0$  at mean sea level (Fig. 1a). The mean water depth is  $h$  with the seabed located at  $z = -h$ . The time coordinate  $t$  starts from  $t = 0$  corresponding to 1 August 2006 (UTC). Bathymetry  $h(x, y)$  at all locations (midshelf to surfzone, Fig. 1) is given by the NOAA Tsunami Digital Elevation Model (DEM) with 9-m spatial resolution (Caldwell et al. 2011). Moorings consisting of ADCP current meters and thermistors were deployed on a cross-shore transect in water depths of 26, 20, 10, and 8 m (hereinafter denoted as M26, M20, M10, M8, respectively) from August to October 2006 (see Fig. 1c, Table 1). Note velocity depth resolution at M26 is coarse, with velocity measurements at only three vertical locations (Fig. 1c). Wind velocity measurements during the experiment were obtained from a meteorological station at N20 (Fig. 1b).

### b. Methods

Observed velocities and temperatures were hourly averaged. In addition, the observed velocities were rotated into HB06 coordinate system cross-shore ( $u$ ) and alongshore ( $v$ ). Observed and modeled velocities and temperature are decomposed into four frequency bands (shaded regions in Fig. 3) using a PL64 filter (Limeburner et al. 1985): subtidal (ST,  $<33^{-1}$  cph), diurnal (DU,  $33^{-1}$  to  $16^{-1}$  cph), semidiurnal (SD,  $16^{-1}$  to  $10^{-1}$  cph), and high frequency (HF,  $>10^{-1}$  cph).

The dominant diurnal and semidiurnal frequency-band vertical structure of baroclinic velocity and temperature variability is identified using empirical orthogonal function (hereinafter EOF) analysis. At each mooring the baroclinic velocity ( $u_{bc}$ ,  $v_{bc}$ ) is defined as the velocity deviation from the depth-averaged velocity, that is,

$$u_{bc}(z, t) = u(z, t) - U(t), \quad (1)$$

where  $U(t)$  is the depth-averaged velocity. Here, as barotropic and baroclinic velocity are similar in magnitude, an EOF analysis on total velocity [i.e.,  $u(z, t)$ ] is not

conducted. Note that in terms of interpretation as internal waves, this baroclinic velocity definition may alias bottom-boundary-layer-induced shear as internal motions (e.g., Edwards and Seim 2008). However, for a consistent analysis of observed and modeled velocity, the baroclinic velocity definition (1) is used. At a mooring location, EOF analysis separates the temporal  $[A^{(n)}(t)]$  and vertical  $[\phi^{(n)}(z)]$  variability into orthogonal modes, such that

$$F(z, t) = \sum_{n=1}^N A^{(n)}(t)\phi^{(n)}(z), \quad (2)$$

where  $F$  is either velocity or temperature,  $N$  is the total number of vertical measurement elevations, and the  $n = 1$  mode has the most variance. Complex baroclinic velocity ( $w_{bc} = u_{bc} + iv_{bc}$ , where  $i = \sqrt{-1}$ ) is subjected to complex EOF (cEOF) analysis (Kundu and Allen 1976), resulting in complex cEOF spatial and temporal modes. Hereinafter, cEOF refers to complex velocity EOF and (c)EOF refers to both complex velocity and temperature EOFs. This (c)EOF decomposition is performed on diurnal- and semidiurnal-band baroclinic velocity and temperatures [i.e.,  $[\phi_{w,DU}^{(1)}(z), \phi_{T,DU}^{(1)}(z)]$  and  $[\phi_{w,SD}^{(1)}(z), \phi_{T,SD}^{(1)}(z)]$ , respectively]. The methodology of decomposing the raw signal to diurnal and semidiurnal frequency bands followed by (c)EOF analysis is analogous to previous studies focused on internal tidal motions (e.g., Lass and Mohrholz 2005; Huan Lee et al. 2012; Bravo et al. 2013). Statistical analysis (spectra or EOF) is performed over each mooring's deployment duration (Table 1). EOF analysis conducted in 5-day increments reveals similar vertical structure and zero crossings as the entire deployment period (not shown).

The diurnal or semidiurnal modeled and observed velocities and temperature corresponding to the EOF mode are reconstructed, such that for diurnal first-mode variables,

$$u_{DU}^{(1)}(z, t) = \text{Re}[A_{w,DU}^{(1)}(t)\phi_{w,DU}^{(1)}(z)], \quad (3a)$$

$$v_{DU}^{(1)}(z, t) = \text{Im}[A_{w,DU}^{(1)}(t)\phi_{w,DU}^{(1)}(z)], \quad \text{and} \quad (3b)$$

$$T_{DU}^{(1)}(z, t) = A_{T,DU}^{(1)}(t)\phi_{T,DU}^{(1)}(z). \quad (3c)$$

This (c)EOF velocity and temperature reconstruction represents vertically coherent variability and is appropriate for internal motions that have a mode structure (i.e., are vertically standing and not vertically propagating). Vertical structure in velocity variability is characterized by velocity variance ellipse major  $U_{\text{maj}}^{(1)}(z)$  and minor  $U_{\text{min}}^{(1)}(z)$  axes estimated from reconstructed  $u^{(1)}(z, t)$  and  $v^{(1)}(z, t)$ . Temperature variability vertical

structure is characterized by first-mode temperature standard deviation (std)  $\sigma_T(z)$ . The velocity mode one cEOF phase  $\theta^{(1)}$  is given by

$$\theta^{(1)} = \tan^{-1} \left\{ \frac{\text{Im}[\phi_{w,DU}^{(1)}]}{\text{Re}[\phi_{w,DU}^{(1)}]} \right\}, \quad (4)$$

which for progressive and standing modal internal motions is expected to vary between  $\pm\pi/2$ .

### 3. Model description, grid setup, and forcing

The Coupled Ocean–Atmosphere–Wave–Sediment Transport (COAWST; Warner et al. 2010) is an open-source modeling system that couples atmospheric (WRF), circulation and stratification (ROMS), wave (SWAN), and sediment transport models. The COAWST modeling system has been applied and validated in a variety of studies, including the study of surfzone (Kumar et al. 2011, 2012) and tidal inlet (Olabarrieta et al. 2011) wave–current interaction; hurricane-forcing-induced exchange between atmosphere, ocean, and surface gravity waves (Olabarrieta et al. 2012); and subtidal circulation from the midshelf to the surfzone (K15). In this study, the coupled ROMS–SWAN mode of COAWST is used. Although wave-induced effects on internal tidal motions are not examined here, the SWAN modeling is briefly presented for completeness. Complete descriptions of these models (i.e., ROMS and SWAN), model setup, grids, forcing, and boundary conditions are given in K15.

The circulation and surface gravity wave dynamics in the HB06 region are simulated using two one-way nested grids L4 and L5. The L4 grid ( $\Delta = 50$  m) spans the shelf break to the inner shelf and surfzone (Fig. 1a) offshore of Huntington Beach and Newport Beach, California, in the SPB with cross-shore and alongshore length scales of 15 and 30 km, respectively. The L4 grid provides information to the innermost L5 grid ( $\Delta = 10$  m) that encompasses the midshelf to the surfzone region, where HB06 instrumentation was located (Fig. 1), and spans approximately 6 km in the alongshore and cross shore (Fig. 1b). Both L4 and L5 grids have 20 bathymetry-following levels. Coupled ROMS–SWAN model simulations from 1 August to 1 November 2006 (92 days) were conducted for both L4 and L5 grids with ROMS baroclinic time steps of 8 and 4 s, respectively, while the barotropic time step was one-twentieth of the baroclinic time step. The SWAN wave action density evolves with time steps of 120 and 60 s for grids L4 and L5, respectively. The SWAN L4 grid lateral boundary wave conditions are obtained from regional deep-water Coastal Data Information Program (CDIP) wave buoy spectra estimates farther offshore. Ray-based spectral

refraction methods (O’Reilly and Guza 1991, 1993) are used to transform these estimates to the boundary. The L4 ROMS boundary conditions are provided by the grid system used by Uchiyama et al. (2014, hereinafter U14), which downscales with four grids from the eastern Pacific (5-km resolution) to the San Pedro shelf (75-m resolution).

Wind forcing is one of the primary circulation drivers in the mid and inner shelf, and accurate wind forcing is critical for simulating nearshore circulation in the Southern California Bight. In this study, WRF-simulated wind stresses are used. Detailed model–data comparison of WRF and measured wind stresses are presented in K15 (see their Fig. 4) with results summarized here. Modeled and observed diurnal wind stresses vary  $\pm 0.03$   $\text{N m}^{-2}$  and are strongly correlated ( $r^2 > 0.65$ ). Observed and modeled subtidal wind stress varies from  $-0.04$  to  $0.05$   $\text{N m}^{-2}$  with moderate correlation in the alongshore ( $r^2 = 0.24$ ) and weak correlation in the cross shore ( $r^2 = 0.07$ ). Differences in observed and modeled wind stresses may occur because of WRF’s coarse resolution (i.e.,  $\Delta = 6$  km) and downscaling effects (from a larger grid) at the land–sea transition.

### 4. Results: Statistical model–data comparison

The SPB mid- to inner-shelf internal wave field is complex because of complicated bathymetry with rapidly varying shelf width over length scales  $>10$  km (Fig. 1). Here, the coupled ROMS–SWAN L5 grid ( $\Delta = 10$  m) model’s ability to simulate the diurnal and semidiurnal internal motions from the mid to inner shelf is tested by statistical model–data comparisons of baroclinic velocities and temperature using spectra and (c)EOF analysis. Superscripts “(m)” and “(o)” denote modeled and observed quantities, respectively. Statistical analysis is performed over the duration of each mooring deployment (Table 1).

#### a. Vertical structure of mean temperature

Mean vertical temperature structure determines water column stratification, influencing the magnitude and the vertical structure of diurnal and semidiurnal internal motions. Salinity-induced density variation is negligible in the SPB (Jones et al. 2002; Wong et al. 2012) and was not measured during the experiment. Vertical profiles of mean temperature were discussed in K15 (see their Fig. 9) but are revisited here (Fig. 2) on the midshelf (M26 and M20) and inner shelf (M10 and M8) to set the stage for diurnal- and semidiurnal-band velocity and temperature structure. Mean mid- and inner-shelf vertical temperature structures were also determined by averaging depth for each isotherm and have an

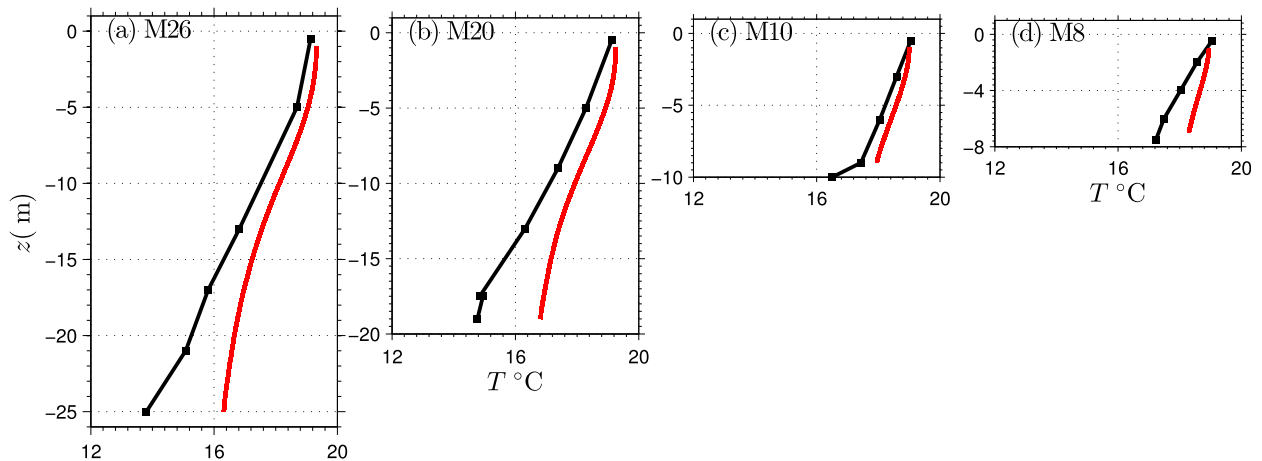


FIG. 2. Observed (black) and modeled (red) vertical profile of mean temperature  $\langle T \rangle$  at (a) M26, (b) M20, (c) M10, and (d) M8. Note the mean is defined over the time data collection occurred at each mooring location (see Table 1).

approximately constant but slightly elevated gradient (not shown).

The mean observed temperature  $\langle T^{(o)} \rangle$  profile varies from  $14^{\circ}$  to  $20^{\circ}\text{C}$  (Figs. 2a–d), while modeled temperature  $\langle T^{(m)} \rangle$  varies from  $16^{\circ}$  to  $20^{\circ}\text{C}$ . Observed and modeled near-surface  $\langle T \rangle$  are similar at all moorings; however, in the rest of the water column, observed  $\langle T^{(o)} \rangle$  is always colder than  $\langle T^{(m)} \rangle$ , which is most evident at the midshelf locations (M26 and M20). The observed mean vertical temperature gradient  $\partial\langle T^{(o)} \rangle/\partial z \approx 0.2^{\circ}\text{C m}^{-1}$  is approximately constant. Modeled vertical mean temperature gradient  $\partial\langle T^{(m)} \rangle/\partial z \approx 0.12^{\circ}\text{C m}^{-1}$  is also approximately constant and about half of that observed (except at M10, Fig. 2c). The relatively weak model stratification possibly occurs because of combination of too weak model stratification inherited from the parent grid solution (i.e., U14) and weak surface forcing (see K15).

### b. Rotary velocity and temperature spectra

Observed and modeled midshelf (i.e., M20) upper-water-column baroclinic velocity ( $u_{bc}$ ,  $v_{bc}$ ) rotary spectra (at  $z = -2$  m), separating clockwise (CW) and counterclockwise (CCW) motions (Gonella 1972), and temperature spectra (at  $z = -5$  m) are estimated (Fig. 3) with a 512-h spectral window (with 50% overlap). This spectral window provides reasonable stability. The frequency resolution ( $\approx 0.0039$  cph) is sufficient to resolve distinct spectral peaks between inertial (0.0462 cph) and diurnal ( $1/24 = 0.0417$  cph) frequencies but is not sufficient to resolve  $K_1$  and  $O_1$  diurnal tidal frequencies. Here, the focus is on the diurnal and semidiurnal bands.

A combination of inertial motions, surface heat flux, and diurnal tidal and wind forcing can lead to baroclinic diurnal-band motions. Midshelf (M20) upper-water-

column DU-band rotary and temperature spectra peak is at the diurnal frequency (i.e., 0.0417 cph) and is a factor of 5–10 weaker at inertial (i.e., 0.0462 cph) frequencies (Figs. 3a,b). The diurnal-band CCW rotary velocity variance is weaker than CW. This CW to CCW asymmetry is similar to sea-breeze-forced diurnal internal motions (e.g., Lerczak et al. 2001). The M20 upper-water-column SD-band baroclinic velocity rotary and temperature spectra peak (Figs. 3a1,a2) is at the M2 tidal frequency, is broader than the DU peak, and is weakly CW/CCW asymmetric. The SD-band broadening (Fig. 3a) is likely due to scattering or Doppler shifting by mesoscale currents (e.g., Colosi et al. 2001; Ward and Dewar 2010; Nash et al. 2012; Dunphy and Lamb 2014).

M20-modeled DU-band rotary spectra favorably compares to the observed by capturing the peak at the diurnal frequency and the CW/CCW asymmetry (red in Fig. 3a). The ratio of CW to CCW integrated DU-band rotary spectra are similar for observed (14) and modeled (20). The modeled SD-band rotary spectra is approximately one-fourth of that observed and also has weak CW/CCW asymmetry (red in Fig. 3a). DU- and SD-band modeled and observed temperature spectra are at the same frequency; however, the modeled is underestimated by a factor of  $\sim 5$  (Fig. 3a2), potentially because of weaker modeled mean stratification (Fig. 2a3). The general underestimation in SD-band baroclinic rotary velocity and temperature spectra is consistent with underestimated barotropic semidiurnal tidal components (see K15).

Given the good DU and SD rotary velocity spectra and reasonable temperature spectra model–data comparison (section 4b), observed and modeled dominant vertical modes of diurnal and semidiurnal velocity and

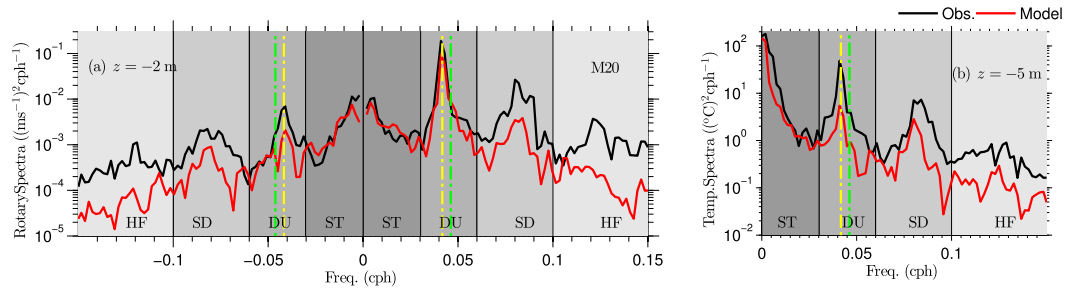


FIG. 3. Observed (black) and modeled (red) baroclinic (a) velocity rotary spectra ( $z = -2$  m) and (b) temperature spectra ( $z = -5$  m) vs frequency for the midshelf M20. For rotary velocity spectra, positive and negative frequencies are clockwise and counterclockwise motions, respectively. The ST ( $<33^{-1}$  cph), DU ( $33^{-1}$  to  $16^{-1}$  cph), SD ( $16^{-1}$  to  $10^{-1}$  cph), and HF ( $>10^{-1}$  cph) bands are indicated. Yellow and green dash-dotted lines are the diurnal ( $1/24$  cph) and inertial ( $1/21.8$  cph) frequencies, respectively.

temperature variability are compared next with the first (c)EOF of velocity and temperature (section 2b) at moorings M26, M20, M10, and M8.

*c. Diurnal baroclinic velocity and temperature: EOF analysis*

Dominant vertical modes of observed and modeled diurnal (DU) baroclinic velocity and temperature variability are compared by the first (c)EOF at the four moorings (M26, M20, M10 and M8). The first cEOF mode well describes the observed and modeled DU baroclinic velocity by explaining between 89% and 95% of the variance (Table 2). The first EOF of observed and modeled temperature explains between 67% and 91% of the variance, with higher values in shallower water depth  $h$  (Table 2). Statistical performance of the model in reproducing the observations is determined through comparison of the first (c)EOF-derived modeled and observed  $U_{\text{maj}}^{(1)}(z)$ ,

$U_{\text{min}}^{(1)}(z)$ , and  $\theta^{(1)}(z)$  for diurnal baroclinic velocity and  $\sigma_T^{(1)}(z)$  for temperature (section 2b).

At all moorings, the first cEOF reconstructed diurnal-band flow is weakly polarized [typically  $U_{\text{maj}}^{(1o)}(z) \approx 1.5\text{--}2 \times U_{\text{min}}^{(1o)}(z)$ ], with  $U_{\text{maj}}^{(1o)}$  typically aligned in the alongshore ( $y$ ) direction (Figs. 4a1,b1,c1,d1). The  $U_{\text{maj}}^{(1o)}(z)$  and  $U_{\text{min}}^{(1o)}(z)$  profiles generally have a near-surface and near-bottom maxima with a midwater column minima, while the observed first cEOF phase  $\theta^{(1o)}$  generally varies from  $-\pi/2$  near the surface to  $+\pi/2$  near the bottom (Figs. 4a2,b2,c2,d2), with the sign change at the  $U_{\text{maj}}^{(1o)}$  minimum location. At all mooring locations, the observed first EOF reconstructed diurnal temperature standard deviation  $\sigma_T^{(1o)}(z)$  varies coherently about  $0.2^\circ\text{--}0.4^\circ\text{C}$  with a midwater column maxima (Figs. 4a3,b3,c3,d3). Although at this latitude diurnal motions are subcritical, the vertical structure of  $U_{\text{maj}}^{(1o)}(z)$ ,  $U_{\text{min}}^{(1o)}(z)$ ,  $\theta^{(1o)}$ , and  $\sigma_T^{(1o)}(z)$  are consistent with a first-mode internal motion.

TABLE 2. Observed and modeled percent variance of first and second mode diurnal and semidiurnal baroclinic velocity CEOF and temperature EOF.

Site	Diurnal band							
	First cEOF vel.		First EOF temp.		Second cEOF vel.		Second EOF temp.	
	Obs.	Model	Obs.	Model	Obs.	Model	Obs.	Model
M26	90	87	67	73	—	—	—	—
M20	89	91	76	83	8	7	13	8
M10	88	93	86	89	—	—	—	—
M8	89	95	91	93	—	—	—	—
Site	Semidiurnal band							
	First cEOF vel.		First EOF temp.		Second cEOF vel.		Second EOF temp.	
	Obs.	Model	Obs.	Model	Obs.	Model	Obs.	Model
M26	74	75	77	71	—	—	—	—
M20	81	74	61	76	13	16	27	12
M10	82	84	77	58	—	—	—	—
M8	84	85	89	75	—	—	—	—

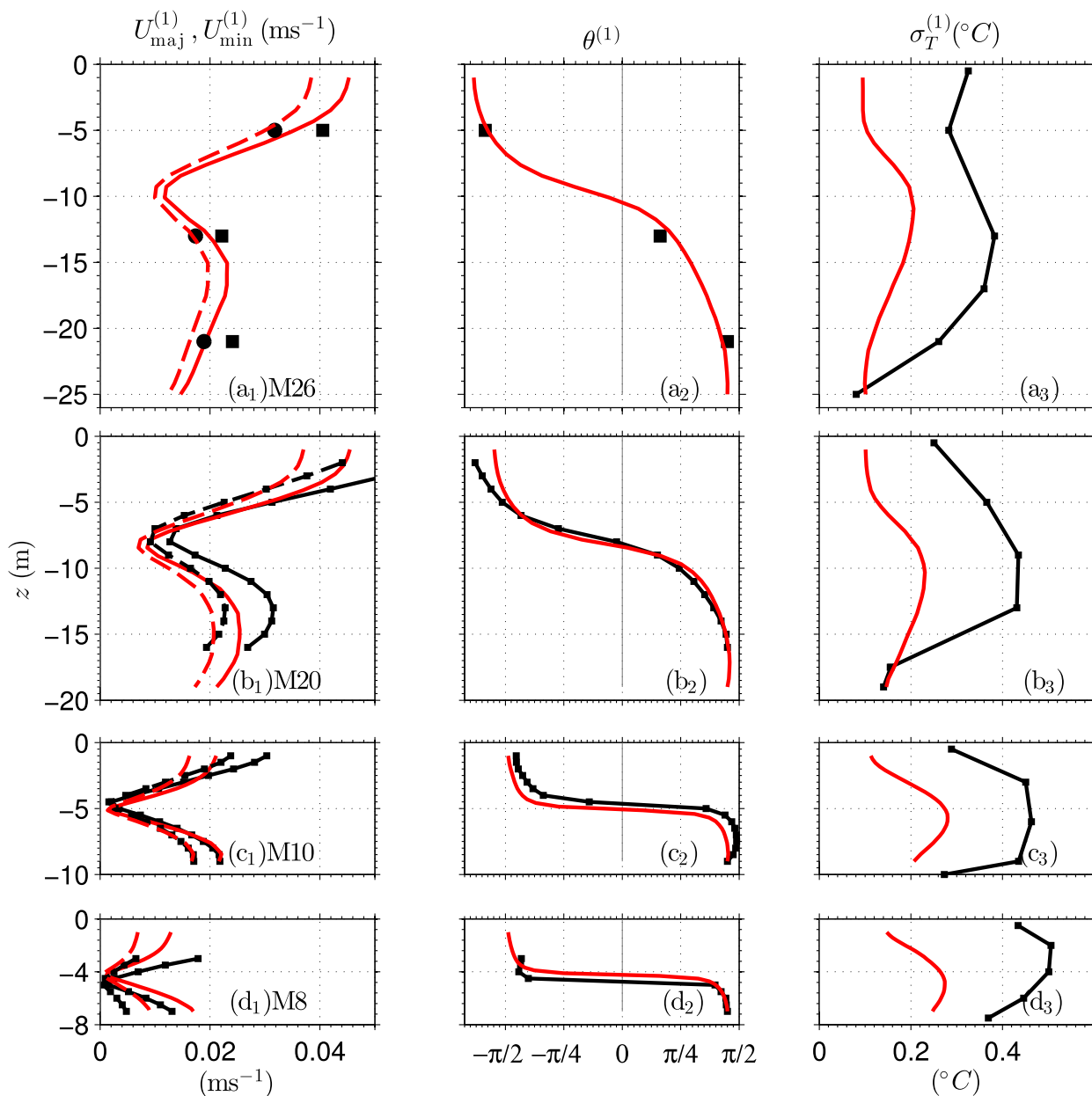


FIG. 4. Vertical ( $z$ ) profiles of first (c)EOF reconstructed diurnal baroclinic velocity and temperature variability for observed (black) and modeled (red) at (top to bottom) midshelf M26 and M20 and inner shelf M10 and M8 sites: (left) the major  $U_{\text{maj}}$  (solid) and minor  $U_{\text{min}}$  (dashed) and (center) phase  $\theta$  of the first diurnal EOF mode  $\phi_{\text{DU}}^{(1)}(z)$ ; (right) standard deviation  $\sigma_T$  of reconstructed diurnal temperature.

The modeled first cEOF reconstructed diurnal  $U_{\text{maj}}^{(1m)}$  and  $U_{\text{min}}^{(1m)}$  vertical structure and magnitude and the modeled first cEOF phase  $\theta^{(1m)}$  are similar to those observed (red curves in Figs. 4a<sub>1</sub>, b<sub>1</sub>, c<sub>1</sub>, d<sub>1</sub> and Figs. 4a<sub>2</sub>, b<sub>2</sub>, c<sub>2</sub>, d<sub>2</sub>). Modeled  $\sigma_T^{(1m)}$  has similar vertical structure to, but is factor of 2 smaller than,  $\sigma_T^{(1o)}$  (Figs. 4a<sub>3</sub>, b<sub>3</sub>, c<sub>3</sub>, d<sub>3</sub>), likely because of weaker model stratification (Fig. 2).

#### d. Semidiurnal baroclinic velocity and temperature: EOF analysis

Observed and modeled vertical structure of SD baroclinic velocity and temperature variability are also compared using the first (c)EOF mode (section 2b) at the four moorings (M26 to M8). The observed and modeled SD baroclinic velocity and temperature are

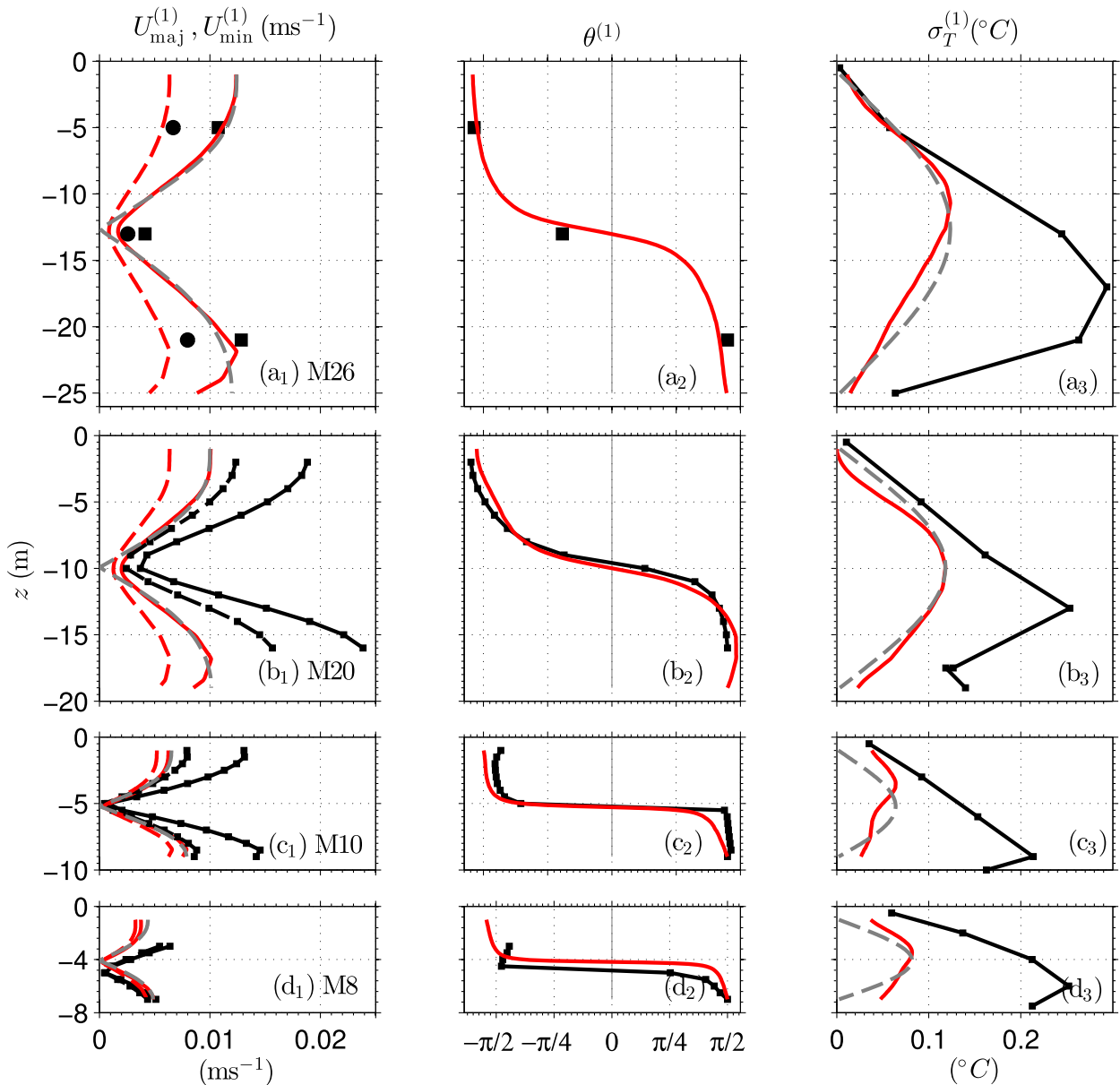


FIG. 5. Vertical ( $z$ ) profiles of first (c)EOF reconstructed semidiurnal baroclinic velocity and temperature variability for observed (black) and modeled (red) at (top to bottom) midshelf M26 and M20 and inner shelf M10 and M8 sites: (left) the major  $U_{\text{maj}}$  (solid) and minor  $U_{\text{min}}$  (dashed) and (center) phase  $\theta$  of the first semidiurnal EOF mode  $\phi_{\text{SD}}^{(1)}(z)$ ; (right) standard deviation  $\sigma_T$  of reconstructed semidiurnal temperature. The dashed gray lines in the left and right panels represent standard deviation of the vertical profile of first mode baroclinic currents and temperature, respectively, multiplied by the maximum magnitude of the major axis and the standard deviation of the reconstructed temperature profile.

well described by the first (c)EOF, explaining between 74% and 95% and between 58% and 93% of the variance, respectively, with slightly higher values in shallower water depth  $h$  (Table 2). As with the diurnal band, the observed and modeled semidiurnal first (c)EOF mode  $U_{\text{maj}}^{(1)}(z)$ ,  $U_{\text{min}}^{(1)}(z)$ ,  $\theta^{(1)}(z)$ , and  $\sigma_T^{(1)}(z)$  are compared.

From M26 to M10 the semidiurnal-band flow is weakly polarized [ $U_{\text{maj}}^{(1o)}(z) \approx 1.5\text{--}2 \times U_{\text{min}}^{(1o)}(z)$ ], with

$U_{\text{maj}}^{(1o)}$  typically aligned in the cross-shore ( $x$ ) direction (Figs. 5a<sub>1</sub>, b<sub>1</sub>, c<sub>1</sub>, d<sub>1</sub>). At M8, semidiurnal baroclinic velocities are not polarized [ $U_{\text{maj}}^{(1o)}(z) \approx U_{\text{min}}^{(1o)}(z)$ ]. The semidiurnal  $U_{\text{maj}}^{(1o)}(z)$  and  $U_{\text{min}}^{(1o)}(z)$  generally have near-surface and near-bottom maxima with a midwater column minima. The observed semidiurnal first cEOF phase  $\theta^{(1o)}$  generally varies from  $-\pi/2$  near the surface to  $+\pi/2$  near the bottom (Figs. 5a<sub>2</sub>, b<sub>2</sub>, c<sub>2</sub>, d<sub>2</sub>), with the

$\theta^{(1o)}$  sign change at the location of the  $U_{\text{maj}}^{(1o)}$  minimum. The observed first EOF reconstructed semidiurnal temperature standard deviation  $\sigma_T^{(1o)}(z)$  varies from 0° to 0.3°C and has roughly parabolic shape with maxima in the lower half of the water column (Figs. 5a<sub>3</sub>, b<sub>3</sub>, c<sub>3</sub>, d<sub>3</sub>). In general, the semidiurnal  $U_{\text{maj}}^{(1o)}(z)$ ,  $U_{\text{min}}^{(1o)}(z)$ ,  $\theta^{(1o)}$ , and  $\sigma_T^{(1o)}(z)$  vertical structure are consistent with a mode-one internal wave.

The modeled first cEOF reconstructed semidiurnal  $U_{\text{maj}}^{(1m)}$  and  $U_{\text{min}}^{(1m)}$  vertical profiles, polarization, ellipse orientation, and first cEOF phase  $\theta^{(1m)}$  are similar to the observed (red curves in Figs. 5a<sub>1</sub>, b<sub>1</sub>, c<sub>1</sub>, d<sub>1</sub> and Figs. 5a<sub>2</sub>, b<sub>2</sub>, c<sub>2</sub>, d<sub>2</sub>). However, the  $U_{\text{maj}}^{(1m)}$  magnitude is underestimated by a factor of  $\sim 2$ . Unlike observed  $\sigma_T^{(1o)}(z)$  the modeled  $\sigma_T^{(1m)}(z)$  is symmetric in the water column and is underpredicted by a factor of  $\sim 3$  at all mooring locations (Figs. 5a<sub>3</sub>, b<sub>3</sub>, c<sub>3</sub>, d<sub>3</sub>).

The observed and modeled first (c)EOF semidiurnal baroclinic velocity structure  $U_{\text{maj}}^{(1)}$ ,  $U_{\text{min}}^{(1)}$ ,  $\theta^{(1)}$ , and  $\sigma_T^{(1)}$  is similar to a mode-one finite-depth semidiurnal internal wave. The relationship of this first (c)EOF semidiurnal variability to a mode-one semidiurnal internal wave is examined by determining the first-mode eigenfunction for horizontal velocity and temperature (see appendix) normalized to match the modeled  $U_{\text{maj}}^{(1m)}$  and  $\sigma_T^{(1m)}$ . The modeled first (c)EOF vertical structure is consistent with the theoretical mode-one internal wave (dashed gray, Figs. 5a<sub>1</sub>, b<sub>1</sub>, c<sub>1</sub>, d<sub>1</sub> and Figs. 5a<sub>3</sub>, b<sub>3</sub>, c<sub>3</sub>, d<sub>3</sub>), suggesting that the semidiurnal first (c)EOF closely represents the evolution of the first baroclinic mode internal wave from the midshelf to the inner shelf.

#### e. Diurnal and semidiurnal second (c)EOF mode at M20

Although weak, the second (c)EOF variability (7%–27%, see Table 2) is not insignificant for DU and SD velocity and temperature. Given the good correspondence between the first (c)EOF for velocity and temperature and the mode-one baroclinic structure, a second (c)EOF model–data comparison is performed at M20 to further examine the model’s ability to reproduce realistic mid- to inner-shelf ocean variability. Note that the observed and modeled second (c)EOF results are similar at M10 and M8 (not shown).

The modeled second cEOF reconstructed DU-band  $U_{\text{maj}}^{(2m)}$  and  $U_{\text{min}}^{(2m)}$  are similar to the observations with slightly less magnitude (red and black curves in Fig. 6a<sub>1</sub>). The DU second cEOF phase  $\theta^{(2o)}$  varies from  $+\pi/2$  to  $-\pi/2$  with two sign changes at  $U_{\text{maj}}^{(2o)}$  minima (black curve in Fig. 6a<sub>2</sub>), a pattern reproduced by the modeled DU  $\theta^{(2m)}$  (red curve in Fig. 6a<sub>2</sub>). The M20 EOF DU reconstructed diurnal temperature  $\sigma_T^{(2o)}(z)$  varies from about 0.12°C, with extrema out of phase with

the  $U_{\text{maj}}^{(2o)}$  extrema (Fig. 6a<sub>3</sub>). The modeled DU  $\sigma_T^{(2m)}(z)$  has qualitatively similar structure (red curve Fig. 6a<sub>3</sub>), although with half the magnitude of the observed  $\sigma_T^{(2o)}$ . The observed and modeled  $U_{\text{maj}}^{(2)}(z)$ ,  $U_{\text{min}}^{(2)}(z)$ ,  $\theta^{(2)}(z)$ , and  $\sigma_T^{(2)}(z)$  vertical structures are consistent with a mode-two internal motion, which the model largely reproduces.

At M20, the observed and modeled SD-band second (c)EOF vertical structure is also similar and representative of a mode-two semidiurnal internal wave (Figs. 6b<sub>1</sub>–b<sub>3</sub>). The modeled second cEOF reconstructed SD-band  $U_{\text{maj}}^{(2m)}$  and  $U_{\text{min}}^{(2m)}$  are similar to the observed, with slightly less magnitude (black and red curves in Fig. 6b<sub>1</sub>). The SD second cEOF phase  $\theta^{(2o)}$  varies from  $-\pi/2$  to  $\pi/2$ , transitioning at  $U_{\text{maj}}^{(2o)}$  minima a pattern reproduced in the modeled SD  $\theta^{(2m)}$  (Fig. 6b<sub>2</sub>). The M20 second EOF SD reconstructed temperature  $\sigma_T^{(2o)}(z)$  varies from about 0.008°C, also with extrema out of phase with the  $U_{\text{maj}}^{(2o)}$  extrema (Fig. 6b<sub>3</sub>). The modeled SD  $\sigma_T^{(2m)}(z)$  has qualitatively similar structure to that observed, although with about half the magnitude (red curve Fig. 6a<sub>3</sub>). Last, the semidiurnal second baroclinic mode (see appendix) gives a velocity and temperature vertical structure very similar to the observed  $U_{\text{maj}}^{(2m)}$  and  $\sigma_T^{(2m)}$  (gray dashed curve in Figs. 6b<sub>1</sub>, b<sub>3</sub>), further confirming the link of the SD second (c)EOF to a mode-two internal wave.

## 5. Discussion

### a. Wind-forced resonant diurnal internal motions?

Observed and modeled diurnal baroclinic velocity and temperature variability are similar to a mode-one internal wave (Fig. 4) and are stronger than semidiurnal internal motions (Figs. 3–5). Generally, modeled diurnal baroclinic velocity is  $\sim 80\%$  of those observed (Fig. 4), whereas modeled temperature variability is approximately one-half of those observed, possibly because of weaker (by approximately one-half) model stratification. These observed and modeled diurnal internal motions can occur because of diurnal SLB wind forcing (e.g., Lerczak et al. 2001) or diurnal barotropic tide propagation over topography (e.g., Beckenbach and Terrill 2008). Both diurnal SLB and barotropic diurnal tides are well modeled (see K15), although the modeled diurnal wind stress is underestimated by approximately one-third. Observed and modeled baroclinic velocity rotary spectra and temperature spectra are peaked at the diurnal frequency (yellow dashed line in Fig. 3). As this is both the SLB and barotropic diurnal tidal ( $K_1$  and  $O_1$ ) forcing frequency, these two forcing mechanisms cannot be distinguished from spectra. In addition, the SPB, located north of the critical latitude ( $\sim 30^\circ$ ), has inertial frequency  $f = 0.0462$  cph greater than the

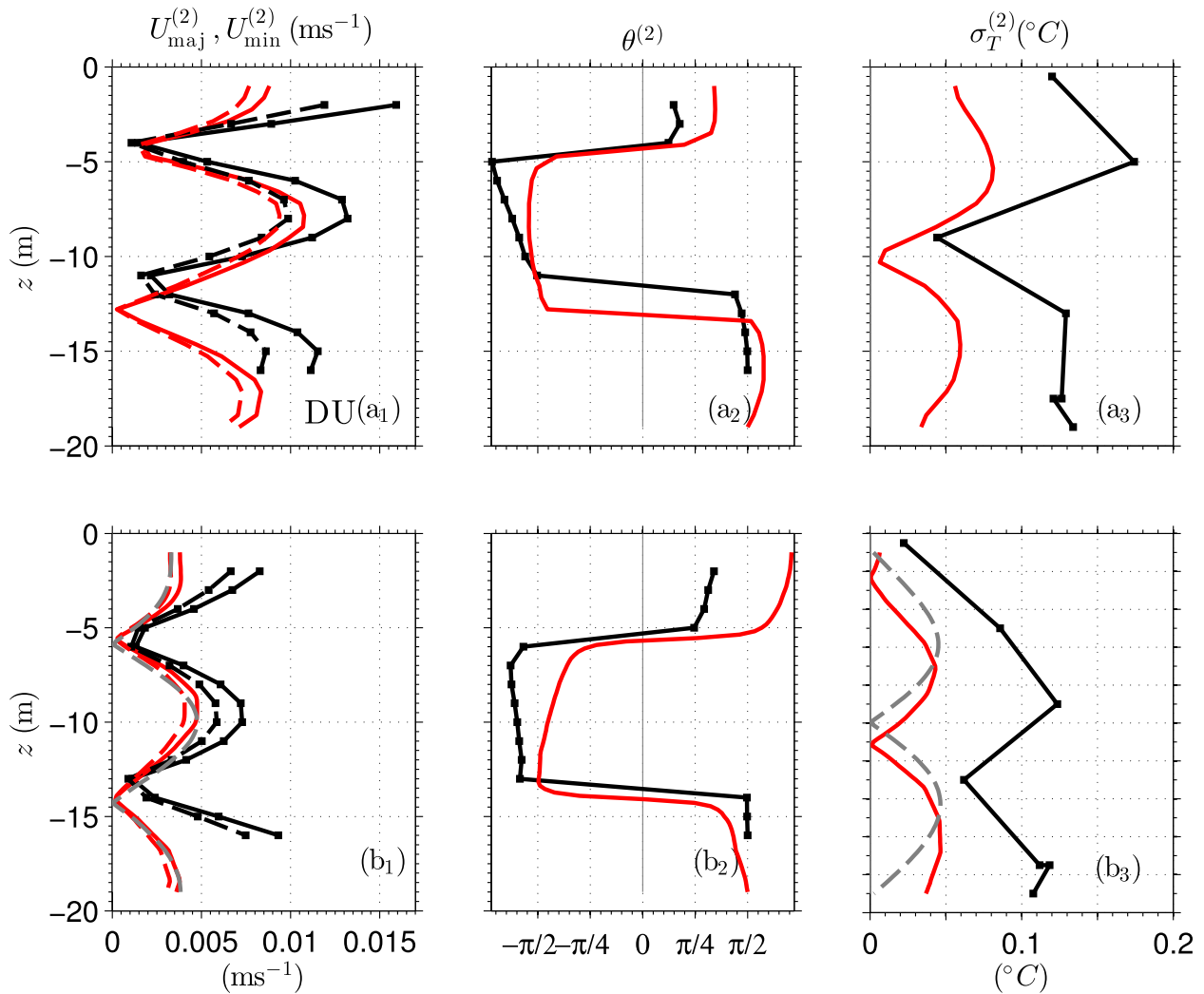


FIG. 6. Vertical ( $z$ ) profiles of second (c)EOF reconstructed (top) diurnal and (bottom) semidiurnal velocity and temperature variability for observed (black) and modeled (red) at midshelf M20: (left) the major  $U_{\text{maj}}$  (solid) and minor  $U_{\text{min}}$  (dashed) and (center) phase  $\theta$  of the second EOF mode; (right) standard deviation  $\sigma_T$  of reconstructed diurnal and semidiurnal temperature. The dashed gray lines in  $b_1$  and  $b_3$  represent standard deviation of the vertical profile of second mode baroclinic currents and temperature, respectively, normalized by the modeled  $U_{\text{maj}}^{(2m)}$  and  $\sigma_T^{(2m)}$ .

diurnal frequency  $\omega_{\text{DU}} = 0.0417$  cph, with diurnal internal motions expected to be evanescent. These observed and modeled diurnal internal motions must either be strongly forced or nonevanescant because of subtidal vorticity, reducing the effective inertial frequency  $f_{\text{eff}} < \omega_{\text{DU}}$  (e.g., Lerczak et al. 2001). Here, the forcing mechanisms and potential resonant response is investigated for observed and modeled diurnal internal motions.

The envelope of observed and modeled bandpassed diurnal wind stress, sea surface elevation, and baroclinic kinetic energy are used to identify the dominant diurnal internal motion-forcing mechanism. A narrow-banded, diurnal signal  $X(t)$  can be represented as

$$X(t) = \hat{X}(\epsilon t) \cos(2\pi\omega_{\text{DU}}t + \theta), \quad (5)$$

where  $\hat{X}$  is the diurnal envelope that varies on longer time scales (written schematically as  $\epsilon t$ ), and  $\theta$  is a random phase. The envelope is estimated by combining the original and Hilbert transformed signal. The diurnal wind stress envelope  $\hat{\tau}_{\text{DU}}$  is the vector magnitude of the cross- and alongshore diurnal wind stress envelopes. Temporal variability in  $\hat{\tau}_{\text{DU}}$  represents longer-term (i.e., subtidal) variability in diurnal wind stress magnitude. The M20 depth-averaged, diurnal baroclinic kinetic energy envelope  $\widehat{\text{KE}}_{\text{DU}}$  is estimated through vector sum of diurnal, bandpassed cross- and alongshore velocity envelopes squared.

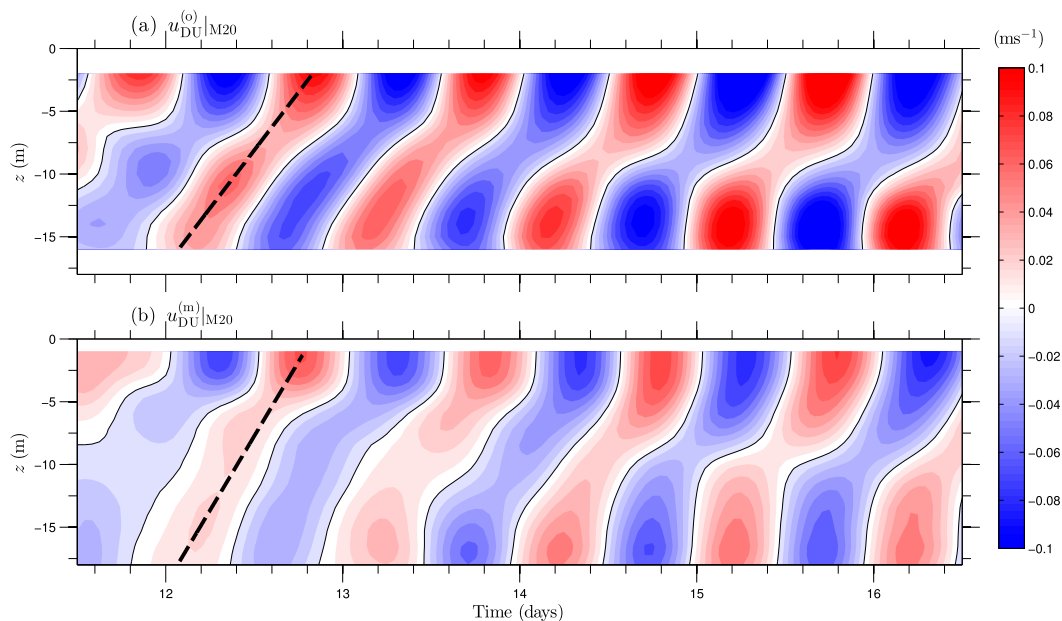


FIG. 7. (a) Observed and (b) modeled bandpassed diurnal, baroclinic, cross-shore ( $u_{DU}$ ) velocities as a function of  $z$  and time at M20. The solid black lines denote zero  $u$ . Black dashed lines have an upward slope of 18.5 and 23  $\text{m day}^{-1}$  for (a) and (b), respectively.

The observed and modeled diurnal barotropic sea surface envelope  $\hat{\xi}_{DU}$  has a  $\sim 14$ -day cycle because of the approximately equal K1 and O1 barotropic tidal components (not shown). Such variability is not seen in either the observed or modeled  $\widehat{KE}_{DU}$ . The  $\hat{\xi}_{DU}$  and  $\widehat{KE}_{DU}$  have squared correlation  $\sim 0$  for both the observed and modeled (not shown), suggesting that these observed and modeled strong diurnal internal motions are not forced by the barotropic tide.

The M20 observed, diurnal-band baroclinic cross-shore velocities  $u_{DU}^{(o)}(z, t)$  (Fig. 7a) have periods of clear upward ( $18.5 \text{ m day}^{-1}$ ) phase propagation (dashed line in Fig. 7a), similar to observations in 70-m water depth near San Diego, California (Lerczak et al. 2001), and 60-m water depth offshore of M20 (Nam and Send 2013). This upward phase propagation is consistent with a downward energy flux, suggesting these diurnal internal motions are surface forced by diurnal winds. Modeled diurnal-band baroclinic cross-shore velocity  $u_{DU}^{(m)}(z, t)$  has similar periods of the upward-phase propagation ( $23 \text{ m day}^{-1}$ , black dashed line, Fig. 7b).

The hourly diurnal wind stress envelope  $\hat{\tau}_{DU}$  and  $\widehat{KE}_{DU}$  have maximum squared correlation  $r^2 \approx 0.22$  when  $\widehat{KE}_{DU}$  is lagged 15 h, consistent with mid- to inner-shelf frictional time scales (e.g., Lentz et al. 1999; K15). Consistent with surface diurnal wind forcing, binned mean  $\hat{\tau}_{DU}$  (lagged by  $-15$  h) and  $\widehat{KE}_{DU}$  are linearly related  $\{[r^{(o)}]^2 = 0.51$  and  $[r^{(m)}]^2 = 0.63\}$  with similar slope in both model and observed (Fig. 8a). This suggests diurnal wind forcing as a

dominant forcing mechanism for the observed and modeled diurnal internal (baroclinic) motions.

However, this location is northward of the critical latitude. Resonant or nonevanescient response to wind forcing is possible poleward of the critical latitude when subtidal vertical vorticity from the depth-averaged subtidal velocity ( $\bar{u}_{ST}$ ,  $\bar{v}_{ST}$ ) reduces the local effective inertial frequency  $f_{\text{eff}} \leq \omega_{DU}$  (e.g., Kunze 1985; Federiuk and Allen 1996; Lerczak et al. 2001; Woodson 2013). Previously, subtidal vorticity modulated diurnal baroclinic kinetic energy enhancement poleward of the critical latitude has been demonstrated only through selected case examples (Lerczak et al. 2001; Nam and Send 2013). The relationship between  $\Gamma = f_{\text{eff}}/f$  and  $\widehat{KE}_{DU}$  at M20 is examined to see whether a resonant wind-forced response can be detected. Following Lerczak et al. (2001),  $f_{\text{eff}}$  is estimated using only  $\partial \bar{v}_{ST}/\partial x$ , that is,

$$f_{\text{eff}} = f + \frac{1}{2} \left( \frac{\partial \bar{v}_{ST}}{\partial x} \right) \quad (6)$$

as modeled  $\partial \bar{u}_{ST}/\partial y \ll \partial \bar{v}_{ST}/\partial x$ , and modeled and observed subtidal velocities have  $\bar{v}_{ST}$  2–4 times stronger than  $\bar{u}_{ST}$  (K15). The observed M20  $\partial \bar{v}_{ST}/\partial x$  is estimated by cross-shore differencing  $\bar{v}_{ST}$  between M10 and M26 ( $\Delta x = 2.1 \text{ km}$ , Fig. 1). Modeled  $\partial \bar{v}_{ST}/\partial x$  is estimated directly at M20. Both modeled and observed  $\partial \bar{v}_{ST}/\partial x$  generally vary from  $\pm 2 \times 10^{-5} \text{ s}^{-1}$  on time scales of 5–10 days (not shown). Subtidal alongshore velocity vertical shear modifications to  $f_{\text{eff}}$  (Kunze 1985; Federiuk

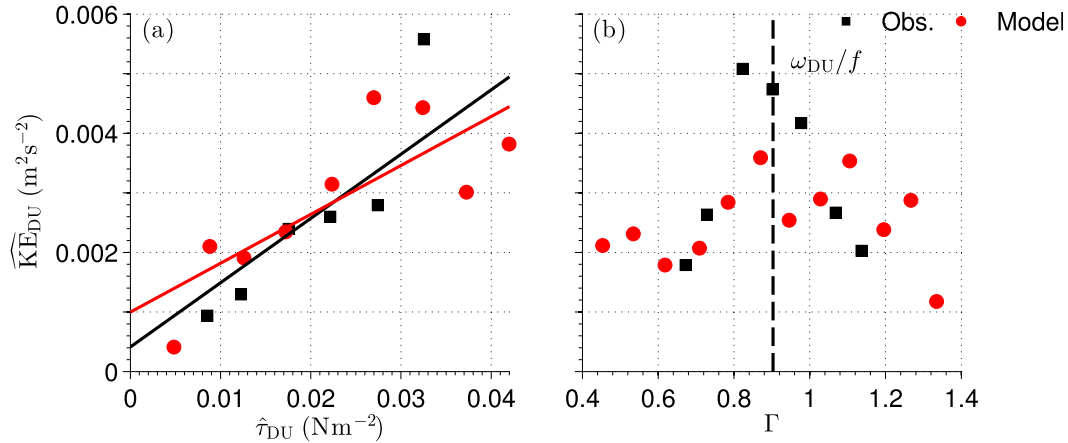


FIG. 8. Observed (black squares) and modeled (red circles) diurnal depth-averaged baroclinic kinetic energy ( $\widehat{KE}_{DU}$ ) vs (a) diurnal wind stress envelope  $\hat{\tau}_{DU}$  (led by 15 h) and (b)  $\Gamma$  [ratio of effective Coriolis frequency to the Coriolis frequency ( $f$ )] at M20. Black dashed vertical lines represent  $\omega_{DU}/f = 0.903$ . The solid lines in (a) are least-squared best-fit lines with slopes 0.11 and 0.08 for observed (black) and modeled (red), respectively.

and Allen 1996) are also small relative to  $\partial\bar{v}_{ST}/\partial x$ . The ratio  $\Gamma = f_{eff}/f$  (similar to Lerczak et al. 2001) is

$$\Gamma = 1 + \frac{1}{2f} \left( \frac{\partial\bar{v}_{ST}}{\partial x} \right). \quad (7)$$

The observed and modeled  $\Gamma$  vary over a similar range from 0.5 to 1.4. In steady-state conditions, for  $\Gamma > \omega_{DU}/f$  (where  $\omega_{DU}/f = 0.90$ ) an evanescent response to diurnal wind forcing is expected; for  $\Gamma \approx \omega_{DU}/f$ , a resonant response is expected; and for  $\Gamma < \omega_{DU}/f$ , a reduced response is expected as the diurnal ( $\omega_{DU}$ ) SLB forcing is off resonance.

The observed and modeled relationship between binned-mean  $\Gamma$  and  $\widehat{KE}_{DU}$  at M20 (Fig. 8b) suggests a subtidal vorticity modulated enhanced response to diurnal forcing (e.g., Lerczak et al. 2001). For  $\Gamma > 1$  and  $\Gamma < 0.8$  when  $f_{eff}$  is not near  $\omega_{DU}$ , observed  $\widehat{KE}_{DU}$  is less than  $0.003 m^2 s^{-2}$  (black squares, Fig. 8b). However, for  $\Gamma \approx 0.9$ , ( $f_{eff} \approx \omega_{DU}$ ) observed  $\widehat{KE}_{DU}$  is maximum with an average of  $0.0047 m^2 s^{-2}$ , suggesting resonant response (Lerczak et al. 2001; Nam and Send 2013). Modeled  $\widehat{KE}_{DU}$  have  $\Gamma$  dependence qualitatively similar to those observed (red circles, Fig. 8b).

The SPB has complex bathymetry, stratification, and diurnal barotropic tidal and wind forcing. The strong relationship between (lagged)  $\hat{\tau}_{DU}$  and  $\widehat{KE}_{DU}$  and the lack of relationship between  $\hat{\zeta}_{DU}$  and  $\widehat{KE}_{DU}$  strongly suggests that the observed and modeled diurnal internal motions are wind forced, which can be enhanced because of subtidal vorticity modulations of the effective inertial frequency. The similarity between the observed and modeled strongly indicates that the model is accurately representing the complex physics resulting in these diurnal internal motions.

*b. Model diurnal vertically integrated heat budget*

Heat budget analysis for synoptic (33–336 h) and fortnightly to longer time scales ( $>336$  h) were examined in K15. Here, the modeled vertically integrated heat budget in the diurnal band is examined. Shortwave solar radiation dominates  $Q_{net}$ ; thus, its variability is largest in the diurnal band. Here, the relative role of diurnal-band advective heat flux divergence versus diurnal-band surface heating in driving modeled diurnal-band temperature variability is examined. The vertically integrated heat budget balances vertically integrated temperature time derivative against surface heat fluxes and the lateral advective heat flux divergence, that is,

$$\int_{-h}^{\bar{\eta}} \frac{\partial T}{\partial t} dz = \frac{Q_{net}}{\rho C_p} - \int_{-h}^{\bar{\eta}} \nabla_H \cdot (\mathbf{u}T) dz, \quad (8)$$

where  $\bar{\eta}$  is the mean sea surface elevation,  $Q_{net}$  is the net (radiative and air–sea) surface heat flux provided by WRF,  $C_p$  is the specific heat capacity of seawater,  $\nabla_H$  is a horizontal divergence, and  $\mathbf{u}$  is the model horizontal velocity vector. The diurnal ( $33^{-1} < \text{Freq.} < 16^{-1}$  cph) components of the three terms in (8) are estimated on the cross-shore instrument transect (Fig. 1) as described in section 2b. The diurnal-band root-mean-square heat budget terms [(8)] as a function of cross-shore coordinate are shown in Fig. 9.

At diurnal time scales, the modeled vertically integrated temperature time derivative ( $\int_{-h}^{\bar{\eta}} \partial T/\partial t dz$ ) and advective heat flux divergences are in balance at all cross-shelf locations from the midshelf to the surfzone, with correlation near one and very similar cross-shelf variability (blue and red lines, Fig. 9a). The modeled

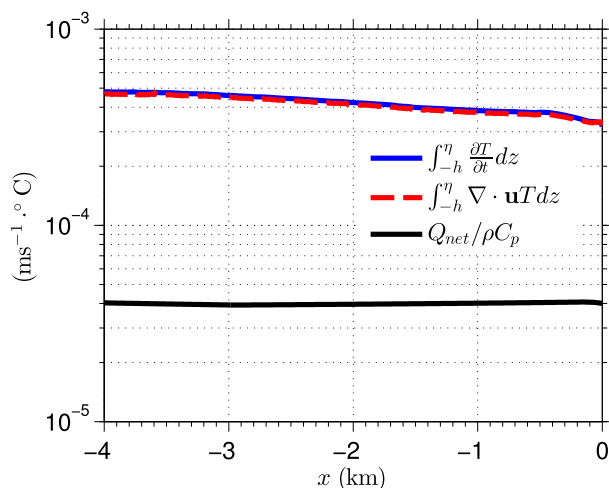


FIG. 9. Root-mean-square of modeled heat budget terms vs cross-shore distance at diurnal ( $16^{-1} < \text{Freq.} < 33^{-1}$  cph) time scales. Heat content time derivative ( $\int_{-h}^{\eta} \partial T / \partial t dz$ ), lateral advective heat flux divergence ( $\int_{-h}^{\eta} \nabla_H \cdot \mathbf{u} T dz$ ), and surface heat flux ( $Q_{\text{net}} / \rho C_p$ ) are indicated in the legend.

surface heat flux term (black line, Fig. 9a) is an order of magnitude smaller from the midshelf to the surfzone, indicating that the vertically integrated heat budget is dominated by advection and not principally due to surface heat flux. The heat budget balance shown in this study is consistent with a local temperature balance between temperature–time derivative and local advection on diurnal time scales in a nearby region of the San Pedro shelf (Boehm et al. 2002). A near-surface heat budget may reveal a stronger contribution of surface heat flux, particularly with respect to the boundary layer mixing and temperature profile. In (8), only the diurnal-band component is estimated. The diurnal velocity and temperature can induce a net heat flux (i.e.,  $u_{\text{DU}} T_{\text{DU}}$ ) at longer time scales, potentially resulting in net warming or cooling, analogous to semidiurnal motions (e.g., Lucas et al. 2011).

### c. Observed and modeled semidiurnal internal wave kinematics

Semidiurnal internal tides cause material exchange between the midshelf and inner shelf (e.g., Lucas et al. 2011; Wong et al. 2012). A realistic numerical model must accurately represent the observed vertical structure, propagation speed, and progressive/standing character of internal tides across these regions to correctly estimate material exchange. The progressive or standing nature of semidiurnal internal tides has been examined through moored observations in submarine canyons (Petruccio et al. 1998), over the outer continental shelf (Savidge et al. 2007) and midshelf (Lerczak et al. 2003). A similar characterization across the

midshelf to inner shelf in both observations and models has not been previously considered.

Both observed and modeled semidiurnal first (c) EOF vertical structure for velocity and temperature are consistent with theoretical mode-one semidiurnal internal waves at all mooring locations (Fig. 5). Additionally, midshelf semidiurnal velocities are cross-shore (+x) polarized (Figs. 5a1–d1), suggesting cross-shore propagation. The progressive or standing nature of the internal tide is diagnosed with cross-spectral analysis (256-h window with 50% overlap) of the semidiurnal first (c) EOF reconstructed velocity and temperature at the farthest offshore (midshelf, M26,  $z = -5$  m) and most inshore (inner shelf, M8,  $z = -2$  m) locations. In both observations and the model, cross-spectral analysis provides temperature–cross-shelf velocity coherence  $C_{Tu}$  and relative phase difference ( $\Delta\theta_{Tu}$ ) in the SD band. The  $\Delta\theta_{Tu}$  distinguishes between progressive ( $\Delta\theta_{Tu} = 0^\circ$ ) and standing ( $\Delta\theta_{Tu} = \pm 90^\circ$ ) mode-one internal waves (Lerczak et al. 2003).

At the midshelf M26 and inner shelf M8, observed  $C_{Tu}^{(o)}$  is maximum ( $\approx 0.8$ ) at the M2 frequency and is reduced at higher and lower frequencies (solid black in Figs. 10a,b). Modeled  $C_{Tu}^{(m)}$  agrees with the observed at M26 and M8 (solid red, Figs. 10a,b). All coherence values are 95% significant. At M26, observed  $\Delta\theta_{Tu}^{(o)} \approx 16^\circ$  and modeled  $\Delta\theta_{Tu}^{(m)} \approx 0^\circ$  over all semidiurnal frequencies (Fig. 10c), indicating a largely progressive mode-one semidiurnal internal tide in both the model and observations. At M8, both observed and modeled  $\Delta\theta_{Tu} \approx 75^\circ$  over the semidiurnal frequency range (Fig. 10d), indicating a transition to a largely standing mode-one semidiurnal internal tide in both model and observations. Between M20 and M8, the phase relationship is neither consistent with a purely progressive or standing wave solution, even though the bottom slope is sub-critical (not shown). In contrast, on a narrower shelf break adjacent to Mission Beach, observed midshelf ( $h = 30$  m)  $\Delta\theta_{Tu} \approx 65^\circ$  (Lerczak et al. 2003), suggesting that the transition from progressive to partially standing occurred farther offshore. Furthermore, the cross-shore polarization of velocity (section 4d) and largely standing phase relationship is not consistent with alongshore-propagating internal edge waves (Lerczak et al. 2003). Overall, even though the progressive to partially standing transition requires further investigation, the mid- and inner-shelf agreement in observed and modeled coherence and phase (Fig. 10) suggests that this nature of the semidiurnal internal tide is well captured by the model.

As the semidiurnal internal waves are predominantly progressive over the midshelf (i.e., M26), the semidiurnal mode-one internal wave phase speed  $c_{\text{SD}}$  is estimated by

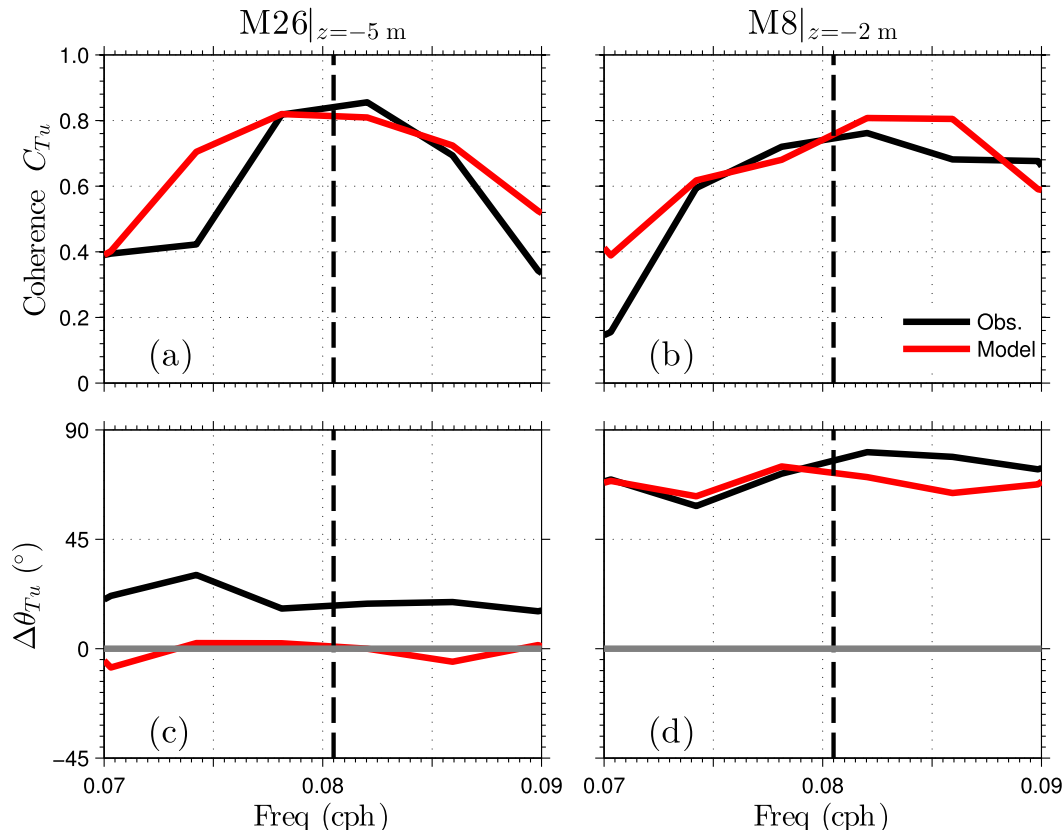


FIG. 10. (top) Coherence  $C_{Tu}$  and (bottom) relative phase  $\Delta\theta_{Tu}$  between first (c) EOF reconstructed temperature  $T$  and cross-shore velocity  $u$  vs frequency in the semidiurnal band (0.07–0.09 cph) for observed (black) and modeled (red) at (a),(c) M26 ( $z = -5$  m) and (b),(d) M8 ( $z = -2$  m). The dashed vertical line is the semidiurnal M2 (0.0805 cph) frequency.

cross-spectral analysis of first cEOF reconstructed cross-shore velocities at M26 and M20 ( $z = -5$  m), which provides the cross-shelf velocity coherence  $C_{uu}$  and the relative phase difference ( $\Delta\theta_{uu}$ ) in the SD band. Observed and modeled coherence  $C_{uu}$  vary similarly from 0.6 to 0.9 within 0.005 cph of the  $M_2$  frequency (Fig. 11a). The observed  $\Delta\theta_{uu}$  varies from  $22^\circ$  to  $30^\circ$  and the modeled  $\Delta\theta_{uu}$  varies from  $30^\circ$  to  $50^\circ$  within 0.005 cph of the  $M_2$  frequency (Fig. 11b), indicating cross-shelf propagation, although at different observed and modeled phase speeds. The observed and modeled near  $M_2$   $\Delta\theta_{uu}$  are converted to a time lag  $\Delta T = T_{M_2} \Delta\theta_{uu} / 360^\circ$ , where  $T_{M_2}$  is the  $M_2$  period, and the mode-one semidiurnal phase speed  $c_{SD} = \Delta x / \Delta T$  with the M26 to M20  $\Delta x = 1100$  m. The M26 to M20 observed  $c_{SD}^{(o)} \approx 0.30 \text{ m s}^{-1}$  is 50% larger than the modeled  $c_{SD}^{(m)} \approx 0.20 \text{ m s}^{-1}$ . As the theoretical mode-one phase speed ( $Nh/\pi$ ) depends linearly on the buoyancy frequency  $N$ , the  $c_{SD}^{(o)}/c_{SD}^{(m)} \approx 1.5$  is consistent with the ratio of observed to modeled  $N^{(o)}/N^{(m)} \approx 1.3$ , where  $N$  is estimated from the mean temperature profiles (Fig. 2). The phase speed estimated from the eigenvalue problem (see appendix) is within

10% of that based on the constant  $N$  theoretical phase speed. The observed and modeled inferred phase speeds are about 1.6 times faster than the theoretical phase speed  $Nh/\pi$  using the observed and modeled  $N$ . In a mixed progressive and standing internal wave field,  $\theta_{uu}$  is expected to be smaller than for a purely progressive field. Similarly, oblique incidence would also reduce  $\Delta\theta_{uu}$ . Both would lead to larger estimated  $c_{SD}$  and potentially explain the weaker theoretical  $c_{SD}$  between M26 and M20.

For a linear, constant  $N$ , mode-one, monochromatic progressive internal wave, the major axis velocity  $U_{maj}^{(1)}$  and standard deviation of temperature  $\sigma_T^{(1)}$  are related such that (e.g., Gill 1982)

$$\frac{(1 - f^2/\omega_{SD}^2)NU_{maj}^{(1)}}{g\alpha\sigma_T^{(1)}} = 1, \tag{9}$$

where  $\omega_{SD} = 0.0805$  cph is the semidiurnal angular frequency and  $\alpha$  is the thermal expansion coefficient. Only M20 was largely consistent with a progressive internal

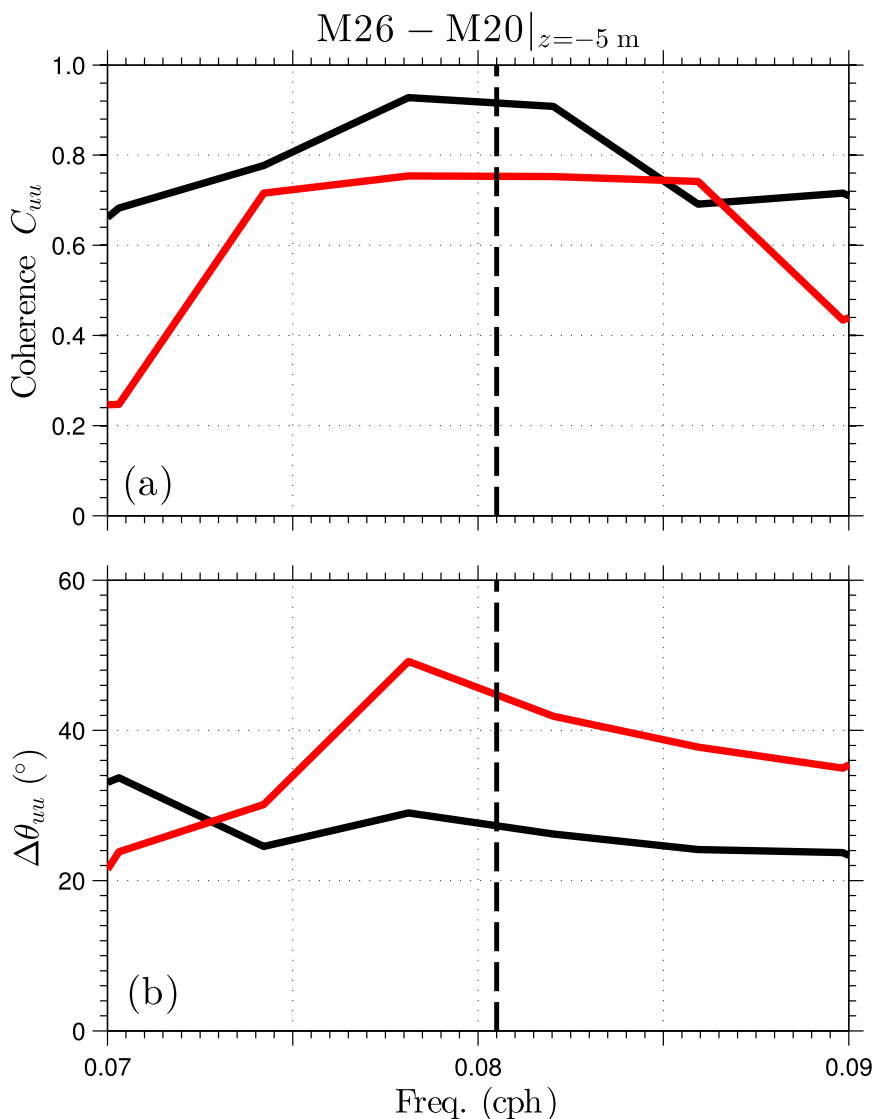


FIG. 11. Observed (black) and modeled (red) (a) coherence  $C_{uu}$  and (b) relative phase  $\Delta\theta_{uu}$  between semidiurnal first (c)EOF reconstructed cross-shore velocities at M26 and M20 vs semidiurnal band frequency (0.07–0.09 cph) at  $z = -5$  m. The dashed vertical line is the semidiurnal M2 (0.0805 cph) frequency.

wave and well-resolved velocity structure (Fig. 5). In both the observations and model, the ratio [(9)] is  $\approx 0.6$ . Observed and modeled ratios [(9)] of  $< 1$  can occur because of a multidirectional (not monochromatic) semidiurnal wave field (e.g., Suanda and Barth 2015), interaction of semidiurnal internal tides with changing stratification (e.g., Rosenfeld 1990), or subtidal currents (Noble et al. 2009), and because of mixed progressive and standing internal wave fields. Alternatively, this standing/progressive analysis could be conducted from the potential to kinetic energy ratio (e.g., Alford and Zhao 2007a) or the perceived group speed (e.g., Alford and Zhao 2007b). Overall, despite differences in observed

and modeled  $U_{\text{maj}}^{(1)}$ ,  $\sigma_T^{(1)}$ , and  $N$ , the observed and modeled semidiurnal internal tide kinematics are similar, indicating that the model is well simulating the semidiurnal internal tide.

#### d. Semidiurnal internal wave variability

Although internal tides can transport material across the near shore (e.g., Wong et al. 2012), their origin is difficult to assess from sparse measurements. The HB06 site has complicated bathymetry associated with many potential local generation sites. The shelf is wider to the northwest (+y) leading into Palos Verdes and narrows from 10 to 2 km to the southeast, with sharp bends and steep, narrow

canyons (Fig. 1). Here, the model is used to determine semidiurnal internal tide temporal variability, delineate regions of local generation and dissipation, and identify multidirectionality of the wave field at the HB06 site.

Semidiurnal baroclinic energy generation, propagation pathways, and dissipation have been extensively studied with ROMS (e.g., Carter et al. 2008; Osborne et al. 2011; Rayson et al. 2012; Buijsman et al. 2012) using a depth-integrated, tidally averaged energy balance given as

$$\frac{\partial E}{\partial t} + \nabla_H \cdot \mathbf{F} = C - D, \quad (10)$$

where  $E$  is the semidiurnal depth-integrated energy (horizontal kinetic plus available potential energy; e.g., Nash et al. 2005),  $\mathbf{F}$  is the depth-integrated baroclinic energy flux,  $C$  represents the semidiurnal barotropic to baroclinic energy conversion, and  $D$  is the semidiurnal internal wave dissipation. In depths  $>100$  m, modeled semidiurnal internal tide generation (positive  $C$ ) is typically balanced by the positive baroclinic energy flux divergence  $\nabla_H \cdot \mathbf{F}$  (e.g., Carter et al. 2008; Buijsman et al. 2012; Osborne et al. 2011). However, the shallower depths of the outer to inner shelf are not considered and a steady-state form of the energy balance (10) is used, neglecting temporal variability.

Here, the temporal variability of modeled, daily averaged midshelf horizontal kinetic energy (HKE) at M20 and the spatial variability of daily averaged baroclinic energy flux  $\mathbf{F}$  and its divergence [(10)] are considered. The model HKE is estimated at M20:

$$\text{HKE} = \frac{\rho_0}{2} \left\langle \int_{-h}^0 u_{\text{SD}}^2 + v_{\text{SD}}^2 dz \right\rangle, \quad (11)$$

where  $u_{\text{SD}}$  and  $v_{\text{SD}}$  are cross- and alongshore bandpassed semidiurnal baroclinic velocities,  $\rho_0 = 1025 \text{ kg m}^{-3}$  is the average density, and  $\langle \rangle$  denotes averaging over two M2 tidal periods ( $\sim 24$  h). Over the L4 model grid (Fig. 1a), the depth-integrated and time-averaged baroclinic energy flux  $\mathbf{F}$  is estimated as

$$\mathbf{F} = \left\langle \int_{-h}^0 \mathbf{u}_{\text{SD}} p_{\text{SD}} dz \right\rangle, \quad (12)$$

where  $p_{\text{SD}}(\hat{z}) = \int_{\hat{z}}^0 g \rho_{\text{SD}}(\hat{z}) d\hat{z} - \int_{z=-h}^0 g \rho_{\text{SD}}(z) dz$  is the baroclinic pressure perturbation whose depth average is zero, that is,  $\int_{z=-h}^0 p_{\text{SD}} dz = 0$  [e.g., Eq. (3) in Nash et al. 2005], and  $\rho_{\text{SD}}$  is the bandpassed semidiurnal baroclinic density perturbation.

Modeled M20 HKE [(11)] varies between 0 and  $6.5 \text{ J m}^{-2}$  on multiday and longer time scales (Fig. 12a), unrelated to the local spring-neap cycle (not shown).

Two 24-h time periods are described in detail. The first, denoted period I, occurred during elevated HKE and large HKE temporal variation (day 11.5–12.5, gray shading in Fig. 12a). The second, denoted period II, corresponds to weak HKE and negligible temporal variation (day 31.5–32.5, yellow shading in Fig. 12b). Given the HKE temporal variability highlighted in periods I and II, the spatial variability of semidiurnal  $\mathbf{F}$  and  $\nabla_H \cdot \mathbf{F}$  [(10)] is examined during periods I and II to determine dominant energy generation and dissipation regions and changes in semidiurnal internal wave directionality.

Period I modeled  $\mathbf{F}$  is strong ( $>1 \text{ W m}^{-1}$ ) and obliquely incident (with respect to the 100-m contour) at the shelf break and in the southern canyon adjacent to Newport Beach (Fig. 12b). At the northwestern canyon ( $x = -8$  km and  $y = 6$  km, Fig. 12b),  $\mathbf{F}$  is  $<0.25 \text{ W m}^{-1}$  and is directed offshore. Period I semidiurnal baroclinic flux divergence  $\nabla_H \cdot \mathbf{F}$  is positive (indicating generation) at the northwestern canyon and also at the shelf break offshore of Huntington Beach (Fig. 12b). At the southern canyon and onshore of the 50-m contour  $\nabla_H \cdot \mathbf{F}$  is negative, associated with energy dissipation. Although  $\nabla_H \cdot \mathbf{F}$  is usually associated with  $C$  or  $D$  in (10), the region adjacent to M26 and M20 has positive  $\nabla_H \cdot \mathbf{F} = -5 \times 10^{-5} \text{ W m}^{-2}$  (Fig. 12b), balanced by the tendency term  $\partial E/\partial t \approx -5 \times 10^{-5} \text{ W m}^{-2}$  at M20. Over a shallow continental shelf unsteady HKE can balance a portion of  $\nabla_H \cdot \mathbf{F}$ .

During period II,  $\mathbf{F}$  varies significantly in magnitude and direction relative to period I. Period II  $\mathbf{F} \approx 0.5 \text{ W m}^{-1}$  and is directed on shore adjacent to the northwestern canyon, is negligible at the shelf break offshore of Huntington Beach, and is directed offshore at the southern canyon off shore of Newport Beach (Fig. 12c). The baroclinic flux divergence  $\nabla_H \cdot \mathbf{F}$  is weak and mostly negative along the shelf break and at the northwestern canyon (Fig. 12b), while strong and positive  $\nabla_H \cdot \mathbf{F}$  ( $3 \times 10^{-4} \text{ W m}^{-2}$ ) is modeled at the southern canyon offshore of Newport Beach. In certain regions the sign of  $\nabla_H \cdot \mathbf{F}$  is switched between periods I and II, potentially indicating a transition from generation to dissipation regions.

These period I and II examples of  $\mathbf{F}$  and  $\nabla_H \cdot \mathbf{F}$  variability illustrate the complex, multidirectional, variable remote and locally generated semidiurnal internal tide in the SPB. In this study, modeled semidiurnal internal tide associated velocity and temperature variability in the mid and inner shelf is approximately one-half of the observed (Figs. 3, 5). These two time periods suggest that to accurately model the semidiurnal internal tide would require accurate spatially temporally variable  $\mathbf{F}$  as boundary conditions, accurate representation of variable generation and dissipation, and accurate mean stratification (Fig. 2).

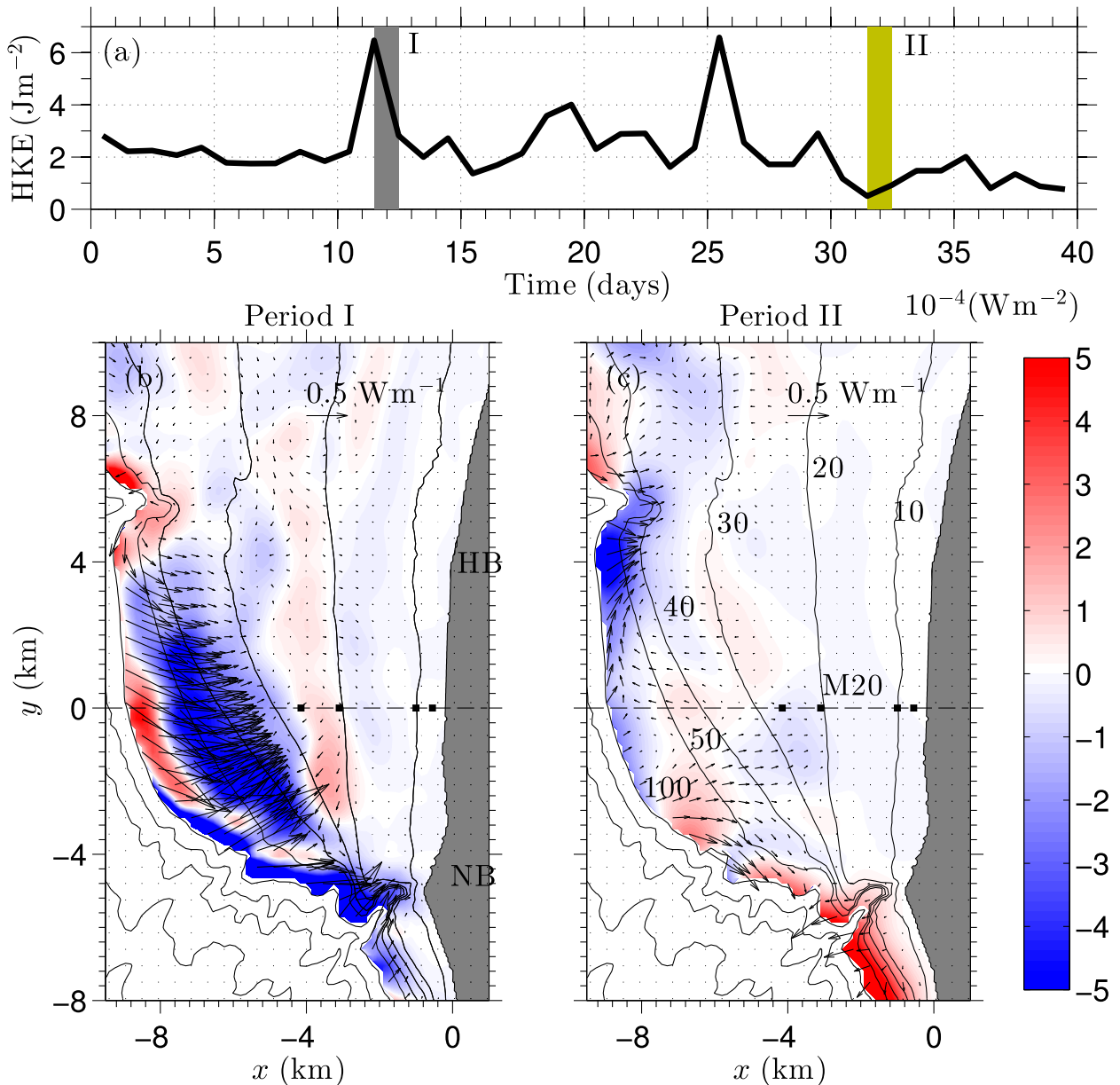


FIG. 12. (a) Modeled 24-h averaged semidiurnal depth-integrated horizontal kinetic energy HKE (11) vs time at M20 with periods of strong HKE (denoted I, gray, 11.5–12.5 days) and weak HKE (denoted II, yellow, 31.5–32.5 days) highlighted. (b),(c) Modeled baroclinic energy flux  $\mathbf{F}$  (arrows) and energy flux divergence  $\nabla_H \cdot \mathbf{F}$  (shading) vs cross-shore  $x$  and alongshore  $y$  coordinate in  $h < 100$  m for (b) period I and (c) period II highlighted in (a). Gray patch represents land, solid black lines are depth contours, and black squares are moorings M26, M20, M10, and M8.

## 6. Summary

Accurately simulating cross-shelf exchange across the midshelf to the inner shelf requires that diurnal and semidiurnal internal motions are correctly represented. Recently, a coupled ROMS–SWAN model, with boundary conditions inherited from a suite of nested models scaling out to the eastern Pacific, was tested on subtidal time scales from the surfzone to the midshelf region

adjacent to Huntington Beach, California, in the San Pedro Bay (K15). Here, the ability of the coupled ROMS–SWAN model to simulate internal variability is examined through statistical comparison to field measurements in the diurnal ( $33^{-1}$  to  $16^{-1}$  cph) and semidiurnal band ( $10^{-1}$  to  $16^{-1}$  cph).

Observed and modeled, time-averaged temperature vertical profiles are linear, although modeled vertical stratification is weaker (approximately one-half) than

observed. Modeled and observed, midshelf, upper-water-column baroclinic velocity rotary spectra agree well in the diurnal band, but modeled is underestimated in the semidiurnal band. Both observed and modeled diurnal-band baroclinic velocities are strongly clockwise-polarized, with similar clockwise to counterclockwise energy ratio. Modeled and observed upper-water-column temperature spectra have similar structure in the diurnal and the semidiurnal band, but the modeled is weaker. The observed first (c) EOF reconstructed (dominant) diurnal velocity and temperature vertical structure are qualitatively similar to a mode-one internal wave, which is reproduced by the model, albeit with weaker (0.5 times) temperature variability. Semidiurnal-band modeled first (c) EOF reconstructed velocity and temperature are similar to observations, but with a weaker magnitude (0.5 times for velocity and 0.33 times for temperature) and a vertical structure consistent with a mode-one internal wave. Furthermore, in the midshelf modeled and observed second (c) EOF, reconstructed diurnal and semidiurnal velocity and temperature have similar vertical structure, with modeled vertical profiles in close agreement with the theoretical second-mode semidiurnal internal wave.

Diurnal barotropic sea surface and diurnal baroclinic kinetic energy envelope are negligibly correlated. Upward phase propagation (i.e., downward energy flux) in the observed and modeled diurnal baroclinic cross-shore velocities and strong correlation between diurnal baroclinic kinetic energy and the wind-forcing envelope in both observed and modeled suggests wind forcing is the dominant mechanism for diurnal internal motions. These internal motions are enhanced by subtidal vorticity-induced reduction in the effective inertial frequency similarly in both the observations and modeled. On diurnal time scales the vertically integrated heat budget is a balance between temperature time derivative and advective heat flux divergence at all mid- and inner-shelf locations, with surface heat flux an order of magnitude smaller.

Observed and modeled semidiurnal temperature-velocity phase is indicative of a largely progressive mode-one internal wave in the midshelf and a largely standing wave on the inner shelf. The ratio of observed to modeled inferred phase speed is consistent with the observed to modeled stratification ratio, as expected from the theoretical linear phase speed. In addition, the ratio of dominant velocity and temperature variability in both observed and modeled are similar and compare well to the theoretical ratio for mode-one progressive internal waves. The significant spatial variability of averaged modeled semidiurnal baroclinic energy flux and its divergence in the San Pedro Bay suggests that the shelf-break region characterized by canyons and kinks on the northwestern and southeastern edges has

complex, multidirectional, variable remote and locally generated semidiurnal internal tide.

Overall, diurnal and semidiurnal baroclinic processes on the mid to inner shelf are consistent between observations on the San Pedro Shelf and a coupled ROMS-SWAN model. This demonstrates that a coupled ROMS-SWAN model can properly represent the diurnal and semidiurnal internal processes across this region. Improved modeled performance would require accurate mean stratification, barotropic and baroclinic boundary fluxes from the parent grid, atmospheric fluxes, and wind forcing adjacent to the land-sea interface.

*Acknowledgments.* Support for N. Kumar and F. Feddersen was provided by the Office of Naval Research (ONR). J. McWilliams was supported by ONR Grant N000141410626 and National Science Foundation Grant OCE-1355970. Y. Uchiyama acknowledges grant-in-aid for scientific research C24560622. Data for the HB06 experiment were obtained within the framework of the Southern California Coastal Ocean Observing System (SCCOOS), National Oceanic and Atmospheric Administration (NOAA), Orange County Sanitation District (OCSD), and United States Geological Survey (USGS) programs at Huntington Beach. Thank you to George Robertson and Marlene Noble for the moored instrument data, and to CDIP and CA State Parks Division of Boating and Waterways for the wave data. B. Woodward, B. Boyd, K. Smith, D. Darnell, I. Nagy, D. Clark, M. Omand, M. Rippey, M. McKenna, M. Yates, R.T. Guza, and D. Michrowski provided field support. W. O'Reilly, Corey Olfe, Daniel Dauhajre, and Florian Lemarie prepared the boundary condition information required for model simulations. Computational support was provided by the COMPAS/ATLAS cluster maintained by Caroline Papadopoulos and Bruce Cornuelle. M. S. Spydell and Bruce Cornuelle provided useful feedback.

## APPENDIX

### Semidiurnal Internal Wave Normal Modes

Modeled baroclinic semidiurnal variability is isolated through a modal decomposition technique (Rayson et al. 2012) obtained by projection of velocity and displacement data onto a vertical internal wave mode. These wave modes are defined as solution to a Sturm-Liouville eigenvalue problem for a vertical structure function  $[\Psi_n(z)]$  corresponding to linear, nonhydrostatic, flat-bottom modes (i.e.,  $n$ ) at each mooring location:

$$\frac{\partial^2 \Psi_n(z)}{\partial z^2} + k_n^2 \frac{N^2 - \omega^2}{\omega^2 - f^2} \Psi_n(z) = 0, \quad (\text{A1})$$

with boundary conditions  $\Psi = 0$  at  $z = 0, -h$ . The squared Brunt–Väisälä frequency is determined from mean temperature profiles. The vertical function  $\Psi_n(z)$  represents the vertical velocity and temperature structure, while the horizontal velocity vertical structure  $U_n(z)$  is  $1/k_n \partial \Psi_n / \partial z$ .

The vertical structures of first and second semidiurnal EOF mode reconstructed velocity and temperature (Figs. 5, 6) are compared to the horizontal velocity and temperature vertical structures  $U_n(z)$  and  $\Psi_n(z)$  by multiplying them to the maximum magnitude of  $U_{\text{maj}}(z)$  and  $\sigma_T(z)$ , respectively.

## REFERENCES

- Alford, M. H., and Z. Zhao, 2007a: Global patterns of low-mode internal-wave propagation. Part I: Energy and energy flux. *J. Phys. Oceanogr.*, **37**, 1829–1848, doi:10.1175/JPO3085.1.
- , and —, 2007b: Global patterns of low-mode internal-wave propagation. Part II: Group velocity. *J. Phys. Oceanogr.*, **37**, 1849–1858, doi:10.1175/JPO3086.1.
- Anderson, D. M., 2009: Approaches to monitoring, control and management of harmful algal blooms (HABs). *Ocean Coastal Manage.*, **52**, 342–347, doi:10.1016/j.ocecoaman.2009.04.006.
- Austin, J. A., and S. J. Lentz, 2002: The inner shelf response to wind-driven upwelling and downwelling. *J. Phys. Oceanogr.*, **32**, 2171–2193, doi:10.1175/1520-0485(2002)032<2171:TISRTW>2.0.CO;2.
- Beckenbach, E., and E. Terrill, 2008: Internal tides over abrupt topography in the Southern California Bight: Observations of diurnal waves poleward of the critical latitude. *J. Geophys. Res.*, **113**, C02001, doi:10.1029/2006JC003905.
- Boehm, A., B. Sanders, and C. Winant, 2002: Cross-shelf transport at Huntington Beach. Implications for the fate of sewage discharged through an offshore ocean outfall. *Environ. Sci. Technol.*, **36**, 1899–1906, doi:10.1021/es0111986.
- Bravo, L., M. Ramos, M. Sobarzo, O. Pizarro, and A. Valle-Levinson, 2013: Barotropic and baroclinic semidiurnal tidal currents in two contrasting coastal upwelling zones of Chile. *J. Geophys. Res. Oceans*, **118**, 1226–1238, doi:10.1002/jgrc.20128.
- Buijsman, M., Y. Uchiyama, J. McWilliams, and C. Hill-Lindsay, 2012: Modeling semidiurnal internal tide variability in the Southern California Bight. *J. Phys. Oceanogr.*, **42**, 62–77, doi:10.1175/2011JPO4597.1.
- Caldwell, R., L. Taylor, B. Eakins, K. Carignan, P. Grothe, E. Lim, and D. Friday, 2011: Digital elevation models of Santa Monica, California: Procedures, data sources and analysis. Tech. Memo. NESDIS NGDC-46, 38 pp. [Available online at [http://docs.lib.noaa.gov/noaa\\_documents/NESDIS/NGDC/TM/NOAA\\_TM\\_NESDIS\\_NGDC\\_46.pdf](http://docs.lib.noaa.gov/noaa_documents/NESDIS/NGDC/TM/NOAA_TM_NESDIS_NGDC_46.pdf).]
- Carter, G., and Coauthors, 2008: Energetics of  $M_2$  barotropic-to-baroclinic tidal conversion at the Hawaiian Islands. *J. Phys. Oceanogr.*, **38**, 2205–2223, doi:10.1175/2008JPO3860.1.
- Clark, D. B., F. Feddersen, and R. T. Guza, 2010: Cross-shore surfzone tracer dispersion in an alongshore current. *J. Geophys. Res.*, **115**, C10035, doi:10.1029/2009JC005683.
- , —, and —, 2011: Modeling surfzone tracer plumes: 2. Transport and dispersion. *J. Geophys. Res.*, **116**, C11028, doi:10.1029/2011JC007211.
- Colosi, J. A., R. C. Beardsley, J. F. Lynch, G. Gawarkiewicz, C.-S. Chiu, and A. Scotti, 2001: Observations of nonlinear internal waves on the outer New England continental shelf during the summer Shelfbreak Primer study. *J. Geophys. Res.*, **106**, 9587–9601, doi:10.1029/2000JC900124.
- Cudaback, C. N., and E. McPhee-Shaw, 2009: Diurnal-period internal waves near Point Conception, California. *Estuarine Coastal Shelf Sci.*, **83**, 349–359, doi:10.1016/j.ecss.2008.12.018.
- Dunphy, M., and K. G. Lamb, 2014: Focusing and vertical mode scattering of the first mode internal tide by mesoscale eddy interaction. *J. Geophys. Res. Oceans*, **119**, 523–536, doi:10.1002/2013JC009293.
- Edwards, C. R., and H. E. Seim, 2008: Complex EOF analysis as a method to separate barotropic and baroclinic velocity structure in shallow water. *J. Atmos. Oceanic Technol.*, **25**, 808–821, doi:10.1175/2007JTECHO562.1.
- Feddersen, F., 2012: Observations of the surfzone turbulent dissipation rate. *J. Phys. Oceanogr.*, **42**, 386–399, doi:10.1175/JPO-D-11-082.1.
- , D. B. Clark, and R. T. Guza, 2011: Modeling of surfzone tracer plumes: 1. Waves, mean currents, and low-frequency eddies. *J. Geophys. Res.*, **116**, C11027, doi:10.1029/2011JC007210.
- Federiuk, J., and J. Allen, 1996: Model studies of near-inertial waves in flow over the Oregon continental shelf. *J. Phys. Oceanogr.*, **26**, 2053–2075, doi:10.1175/1520-0485(1996)026<2053:MSONIW>2.0.CO;2.
- Fewings, M. R., and S. J. Lentz, 2011: Summertime cooling of the shallow continental shelf. *J. Geophys. Res.*, **116**, C07015, doi:10.1029/2010JC006744.
- Gill, A. E., 1982: *Atmosphere-Ocean Dynamics*. International Geophysics Series, Vol. 30, Academic Press, 662 pp.
- Gonella, J., 1972: A rotary-component method for analysing meteorological and oceanographic vector time series. *Deep-Sea Res. Oceanogr. Abstr.*, **19**, 833–846, doi:10.1016/0011-7471(72)90002-2.
- Grant, S. B., J. H. Kim, B. H. Jones, S. A. Jenkins, J. Wasyl, and C. Cudaback, 2005: Surfzone entrainment, along-shore transport, and human health implications of pollution from tidal outlets. *J. Geophys. Res.*, **110**, C10025, doi:10.1029/2004JC002401.
- Huan Lee, I., Y.-H. Wang, Y. Yang, and D.-P. Wang, 2012: Temporal variability of internal tides in the northeast South China Sea. *J. Geophys. Res.*, **117**, C02013, doi:10.1029/2011JC007518.
- Huthnance, J., 1989: Internal tides and waves near the continental shelf edge. *Geophys. Astrophys. Fluid Dyn.*, **48**, 81–106, doi:10.1080/03091928908219527.
- Inall, M., D. Aleynik, T. Boyd, M. Palmer, and J. Sharples, 2011: Internal tide coherence and decay over a wide shelf sea. *Geophys. Res. Lett.*, **38**, L23607, doi:10.1029/2011GL049943.
- Jachec, S., O. Fringer, M. Gerritsen, and R. Street, 2006: Numerical simulation of internal tides and the resulting energetics within Monterey Bay and the surrounding area. *Geophys. Res. Lett.*, **33**, L12605, doi:10.1029/2006GL026314.
- Jones, B. H., M. A. Noble, and T. D. Dickey, 2002: Hydrographic and particle distributions over the Palos Verdes Continental Shelf: Spatial, seasonal and daily variability. *Cont. Shelf Res.*, **22**, 945–965, doi:10.1016/S0278-4343(01)00114-5.
- Kumar, N., G. Voulgaris, and J. C. Warner, 2011: Implementation and modification of a three-dimensional radiation stress formulation for surfzone and rip-current applications. *Coastal Eng.*, **58**, 1097–1117, doi:10.1016/j.coastaleng.2011.06.009.
- , —, —, and M. Olabarrieta, 2012: Implementation of the vortex force formalism in the coupled ocean-atmosphere-

- wave-sediment transport (COAWST) modeling system for inner shelf and surfzone applications. *Ocean Modell.*, **47**, 65–95, doi:10.1016/j.ocemod.2012.01.003.
- , F. Feddersen, Y. Uchiyama, J. McWilliams, and W. O'Reilly, 2015: Midshelf to surfzone coupled ROMS–SWAN model–data comparison of waves, currents, and temperature: Diagnosis of subtidal forcings and response. *J. Phys. Oceanogr.*, **45**, 1464–1490, doi:10.1175/JPO-D-14-0151.1.
- Kundu, P. K., and J. Allen, 1976: Some three-dimensional characteristics of low-frequency current fluctuations near the Oregon coast. *J. Phys. Oceanogr.*, **6**, 181–199, doi:10.1175/1520-0485(1976)006<0181:STDCOL>2.0.CO;2.
- Kunze, E., 1985: Near-inertial wave propagation in geostrophic shear. *J. Phys. Oceanogr.*, **15**, 544–565, doi:10.1175/1520-0485(1985)015<0544:NIWPIG>2.0.CO;2.
- Lass, H. U., and V. Mohrholz, 2005: On the fluctuations and vertical structure of the shelf circulation off walvis bay, Namibia. *Cont. Shelf Res.*, **25**, 1473–1497, doi:10.1016/j.csr.2005.04.012.
- Leichter, J. J., S. R. Wing, S. L. Miller, and M. W. Denny, 1996: Pulsed delivery of subthermocline water to Conch reef (Florida Keys) by internal tidal bores. *Limnol. Oceanogr.*, **41**, 1490–1501, doi:10.4319/lo.1996.41.7.1490.
- Lentz, S. J., and M. R. Fewings, 2012: The wind-and wave-driven inner-shelf circulation. *Annu. Rev. Mar. Sci.*, **4**, 317–343, doi:10.1146/annurev-marine-120709-142745.
- , R. T. Guza, S. Elgar, F. Feddersen, and T. H. C. Herbers, 1999: Momentum balances on the North Carolina inner shelf. *J. Geophys. Res.*, **104**, 18 205–18 240, doi:10.1029/1999JC900101.
- Lerczak, J. A., M. Hendershott, and C. Winant, 2001: Observations and modeling of coastal internal waves driven by a diurnal sea breeze. *J. Geophys. Res.*, **106**, 19 715–19 729, doi:10.1029/2001JC000811.
- , C. Winant, and M. Hendershott, 2003: Observations of the semidiurnal internal tide on the southern California slope and shelf. *J. Geophys. Res.*, **108**, 3068, doi:10.1029/2001JC001128.
- Limeburner, R., and Coauthors, 1985: CODE-2: Moored array and large-scale data report. WHOI Tech. Rep. 85-35/CODE Tech. Rep. 38, 233 pp., doi:10.1575/1912/1641.
- Lucas, A., P. Franks, and C. Dupont, 2011: Horizontal internal-tide fluxes support elevated phytoplankton productivity over the inner continental shelf. *Limnol. Oceanogr. Fluids Environ.*, **1**, 56–74, doi:10.1215/21573698-1258185.
- Mackinnon, J. A., and M. C. Gregg, 2003: Mixing on the late-summer New England Shelf solibores, shear, and stratification. *J. Phys. Oceanogr.*, **33**, 1476–1492, doi:10.1175/1520-0485(2003)033<1476:MOTLNE>2.0.CO;2.
- Nam, S., and U. Send, 2011: Direct evidence of deep water intrusions onto the continental shelf via surging internal tides. *J. Geophys. Res.*, **116**, C05004, doi:10.1029/2010JC006692.
- , and —, 2013: Resonant diurnal oscillations and mean alongshore flows driven by sea/land breeze forcing in the coastal Southern California Bight. *J. Phys. Oceanogr.*, **43**, 616–630, doi:10.1175/JPO-D-11-0148.1.
- Nash, J. D., M. H. Alford, and E. Kunze, 2005: Estimating internal wave energy fluxes in the ocean. *J. Atmos. Oceanic Technol.*, **22**, 1551–1570, doi:10.1175/JTECH1784.1.
- , S. M. Kelly, E. L. Shroyer, J. N. Moum, and T. F. Duda, 2012: The unpredictable nature of internal tides on continental shelves. *J. Phys. Oceanogr.*, **42**, 1981–2000, doi:10.1175/JPO-D-12-028.1.
- Noble, M., B. Jones, P. Hamilton, J. Xu, G. Robertson, L. Rosenfeld, and J. Largier, 2009: Cross-shelf transport into nearshore waters due to shoaling internal tides in San Pedro Bay, CA. *Cont. Shelf Res.*, **29**, 1768–1785, doi:10.1016/j.csr.2009.04.008.
- O'Reilly, W., and R. T. Guza, 1991: Comparison of spectral refraction and refraction-diffraction wave models. *J. Waterw. Port Coastal Ocean Eng.*, **117**, 199–215, doi:10.1061/(ASCE)0733-950X(1991)117:3(199).
- , and —, 1993: A comparison of two spectral wave models in the Southern California Bight. *Coastal Eng.*, **19**, 263–282, doi:10.1016/0378-3839(93)90032-4.
- Olabarrieta, M., J. C. Warner, and N. Kumar, 2011: Wave-current interaction in Willapa Bay. *J. Geophys. Res.*, **116**, C12014, doi:10.1029/2011JC007387.
- , —, B. Armstrong, J. B. Zambon, and R. He, 2012: Ocean–atmosphere dynamics during Hurricane Ida and Nor'Ida: An application of the coupled ocean–atmosphere–wave–sediment transport (COAWST) modeling system. *Ocean Modell.*, **43–44**, 112–137, doi:10.1016/j.ocemod.2011.12.008.
- Omand, M. M., J. J. Leichter, P. J. S. Franks, A. J. Lucas, R. T. Guza, and F. Feddersen, 2011: Physical and biological processes underlying the sudden appearance of a red-tide surface patch in the nearshore. *Limnol. Oceanogr.*, **56**, 787–801, doi:10.4319/lo.2011.56.3.0787.
- , F. Feddersen, P. J. S. Franks, and R. T. Guza, 2012: Episodic vertical nutrient fluxes and nearshore phytoplankton blooms in Southern California. *Limnol. Oceanogr.*, **57**, 1673–1688, doi:10.4319/lo.2012.57.6.1673.
- Osborne, J., A. Kurapov, G. Egbert, and P. Kosro, 2011: Spatial and temporal variability of the  $M_2$  internal tide generation and propagation on the Oregon Shelf. *J. Phys. Oceanogr.*, **41**, 2037–2062, doi:10.1175/JPO-D-11-02.1.
- Petruncio, E. T., L. K. Rosenfeld, and J. D. Paduan, 1998: Observations of the internal tide in Monterey Canyon. *J. Phys. Oceanogr.*, **28**, 1873–1903, doi:10.1175/1520-0485(1998)028<1873:OOTTTI>2.0.CO;2.
- Pineda, J., 1994: Internal tidal bores in the nearshore: Warm-water fronts, seaward gravity currents and the onshore transport of neustonic larvae. *J. Mar. Res.*, **52**, 427–458, doi:10.1357/0022240943077046.
- , 1999: Circulation and larval distribution in internal tidal bore warm fronts. *Limnol. Oceanogr.*, **44**, 1400–1414, doi:10.4319/lo.1999.44.6.1400.
- Rayson, M., N. Jones, and G. Ivey, 2012: Temporal variability of the standing internal tide in the Browse Basin, Western Australia. *J. Geophys. Res.*, **117**, C06013, doi:10.1029/2011JC007523.
- Rippy, M. A., P. J. S. Franks, F. Feddersen, R. T. Guza, and D. F. Moore, 2013: Factors controlling variability in nearshore fecal pollution: Fecal indicator bacteria as passive particles. *Mar. Pollut. Bull.*, **66**, 151–157, doi:10.1016/j.marpolbul.2012.09.030.
- Rosenfeld, L. K., 1990: Baroclinic semidiurnal tidal currents over the continental shelf off northern California. *J. Geophys. Res.*, **95**, 22 153–22 172, doi:10.1029/JC095iC12p22153.
- Savidge, D. K., C. R. Edwards, and M. Santana, 2007: Baroclinic effects and tides on the Cape Hatteras continental shelf. *J. Geophys. Res.*, **112**, C09016, doi:10.1029/2006JC003832.
- Simpson, J., P. Hyder, T. Rippeth, and I. Lucas, 2002: Forced oscillations near the critical latitude for diurnal-inertial resonance. *J. Phys. Oceanogr.*, **32**, 177–187, doi:10.1175/1520-0485(2002)032<0177:FONTCL>2.0.CO;2.

- Sinnett, G., and F. Feddersen, 2014: The surfzone heat budget: The effect of wave heating. *Geophys. Res. Lett.*, **41**, 7217–7226, doi:[10.1002/2014GL061398](https://doi.org/10.1002/2014GL061398).
- Suanda, S. H., and J. A. Barth, 2015: Semidiurnal baroclinic tides on the Central Oregon inner shelf. *J. Phys. Oceanogr.*, **45**, 2640–2659, doi:[10.1175/JPO-D-14-0198.1](https://doi.org/10.1175/JPO-D-14-0198.1).
- Uchiyama, Y., E. Y. Idica, J. C. McWilliams, and K. D. Stolzenbach, 2014: Wastewater effluent dispersal in Southern California bays. *Cont. Shelf Res.*, **76**, 36–52, doi:[10.1016/j.csr.2014.01.002](https://doi.org/10.1016/j.csr.2014.01.002).
- Ward, M. L., and W. K. Dewar, 2010: Scattering of gravity waves by potential vorticity in a shallow-water fluid. *J. Fluid Mech.*, **663**, 478–506, doi:[10.1017/S0022112010003721](https://doi.org/10.1017/S0022112010003721).
- Warner, J. C., B. Armstrong, R. He, and J. B. Zambon, 2010: Development of a coupled ocean–atmosphere–wave–sediment transport (COAWST) modeling system. *Ocean Modell.*, **35**, 230–244, doi:[10.1016/j.ocemod.2010.07.010](https://doi.org/10.1016/j.ocemod.2010.07.010).
- Winant, C. D., and A. W. Bratkovich, 1981: Temperature and currents on the Southern California Shelf: A description of the variability. *J. Phys. Oceanogr.*, **11**, 71–86, doi:[10.1175/1520-0485\(1981\)011<0071:TACOTS>2.0.CO;2](https://doi.org/10.1175/1520-0485(1981)011<0071:TACOTS>2.0.CO;2).
- Wong, S. H. C., A. E. Santoro, N. J. Nidzieko, J. L. Hench, and A. B. Boehm, 2012: Coupled physical, chemical, and microbiological measurements suggest a connection between internal waves and surfzone water quality in the Southern California Bight. *Cont. Shelf Res.*, **34**, 64–78, doi:[10.1016/j.csr.2011.12.005](https://doi.org/10.1016/j.csr.2011.12.005).
- Woodson, C. B., 2013: Spatiotemporal variation in cross-shelf exchange across the inner shelf of Monterey Bay, California. *J. Phys. Oceanogr.*, **43**, 1648–1665, doi:[10.1175/JPO-D-11-0185.1](https://doi.org/10.1175/JPO-D-11-0185.1).
- Zhang, X., S. F. DiMarco, D. C. Smith IV, M. K. Howard, A. E. Jochens, and R. D. Hetland, 2009: Near-resonant ocean response to sea breeze on a stratified continental shelf. *J. Phys. Oceanogr.*, **39**, 2137–2155, doi:[10.1175/2009JPO4054.1](https://doi.org/10.1175/2009JPO4054.1).
- , D. C. Smith IV, S. F. DiMarco, and R. D. Hetland, 2010: A numerical study of sea-breeze-driven ocean Poincare wave propagation and mixing near the critical latitude. *J. Phys. Oceanogr.*, **40**, 48–66, doi:[10.1175/2009JPO4216.1](https://doi.org/10.1175/2009JPO4216.1).